Bioorganic & Medicinal Chemistry 28 (2020) 115252

Contents lists available at ScienceDirect

Bioorganic & Medicinal Chemistry

journal homepage: www.elsevier.com/locate/bmc

Discovery of 1,2,4-oxadiazole derivatives as a novel class of noncompetitive inhibitors of 3-hydroxykynurenine transaminase (HKT) from *Aedes aegypti*

Larissa G. Maciel[a], Andrew A. Oliveira[b], Tatiany P. Romão[c], Laylla L.L. Leal[a], Rafael V.C. Guido[b], Maria Helena N.L. Silva-Filha[c], Janaína V. dos Anjos[a,*], Thereza A. Soares[a,*]

[a] Department of Fundamental Chemistry – Federal University of Pernambuco, Av. Jornalista Aníbal Fernandes, s/n°Cidade Universitária – Recife, PE 50740-560, Brazil
[b] Sao Carlos Institute of Physics – University of São Paulo, Av. Joao Dagnone, 1100 Jardim Santa Angelina, São Carlos, SP 13563-120, Brazil
[c] Institute Aggeu Magalhães (IAM) – FIOCRUZ, Av. Professor Moraes Rego s/n°, Recife, PE 50740-560 Brazil

ARTICLE INFO

Keywords:
Kinetic constants
New HKT recombinant
Expression in *Escherichia coli*
Xanthurenic acid detection

ABSTRACT

The mosquito *Aedes aegypti* is the vector of arboviruses such as Zika, Chikungunya, dengue and yellow fever. These infectious diseases have a major impact on public health. The unavailability of effective vaccines or drugs to prevent or treat most of these diseases makes vector control the main form of prevention. One strategy to promote mosquito population control is the use of synthetic insecticides to inhibit key enzymes in the metabolic pathway of these insects, particularly during larval stages. One of the main targets of the kynurenine detoxification pathway in mosquitoes is the enzyme 3-hydroxykynurenine transaminase (HKT), which catalyzes the conversion of 3-hydroxykynurenine (3-HK) into xanthurenic acid (XA). In this work, we report eleven newly synthesized oxadiazole derivatives and demonstrate that these compounds are potent noncompetitive inhibitors of HKT from *Ae. aegypti*. The present data provide direct evidence that HKT can be explored as a molecular target for the discovery of novel larvicides against *Ae. aegypti*. More importantly, it ensures that structural information derived from the HKT 3D-structure can be used to guide the development of more potent inhibitors.

1. Introduction

Arboviruses are responsible for diseases such as Zika, Chikungunya, dengue and yellow fever which have spread at high rates throughout the world in the last years.[1–4] Therefore, increasing mortality and morbidity rates have been reported in association with these diseases.[5–8] More recently, Zika viruses have spread around the world, with a particularly aggravating effect of the congenital syndrome in newborns whose mothers were infected in pregnancy.[9,10] The World Health Organization have reported the Zika virus transmission in 52 countries and territories of the Americas between 2015 and 2018, and 31 countries worldwide have reported infantile microcephaly and/or CNS malformation cases until March 2017.[11,12]

The mosquito *Aedes aegypti* is the primary vector responsible for the transmission of the Zika, hikungunya and dengue viruses. The control of this species has been impaired due to the great adaptability of the mosquito to urban environments, high anthropophilic behavior in addition to other biological features.[2,13] Moreover, vaccine development against all arboviruses and their multiple serotypes transmitted by a given vector has a high cost and requires exceedingly long periods of development.[14,15] In the absence of effective vaccines, the most accessible alternative to decrease the transmission of these diseases remains vector control. In this scenario, the discovery of novel insecticides with innovative mode of action is needed, in particular, in view of the spread resistance to synthetic compounds such as organophosphates and pyrethroids, which have been largely employed against *Ae. aegypti* control.[16–19] Nowadays the mosquito mechanism of resistance is better understood.[20–22] It is known that insects can become insensitive to insecticide through metabolic resistance in which insecticide-resistant strains metabolize the insecticide more efficiently than insecticide-susceptible strains, and/or through target modification in which the insecticide-target molecule may change the structure/sequence or even behavioral modifications with indoor feeders becoming outdoor feeders. Therefore, it is indispensable for novel larvicides to exhibit high specificity and low toxicity in order to minimize the emergence of resistant mosquitoes and toxic effects in other species.[20]

An important metabolic pathway in mosquitoes is the kynurenine pathway, which is the major tryptophan catabolism pathway in living organisms. The tryptophan can be oxidized to quinolinic acid, kynurenic acid, or xanthurenic acid depending on the organism.[23–25] In humans, some metabolites from this pathway are involved in several neurologic disorders and the quinolinic acid can react to form

* Corresponding authors.
E-mail addresses: janaina.anjos@ufpe.br (J.V. dos Anjos), thereza.soares@ufpe.br (T.A. Soares).

https://doi.org/10.1016/j.bmc.2019.115252
Received 14 August 2019; Received in revised form 5 December 2019; Accepted 5 December 2019
Available online 09 December 2019
0968-0896/

nicotinamide adenine dinucleotide (NAD+).[25,26] The metabolite 3-hydroxykynurenine (3-HK) has been associated with oxidative stress caused by spontaneous oxidation of reactive oxygen species.[27,28] In this case, 3-HK can be either hydrolyzed by the enzyme kynureninase or can be the precursor for xanthurenic acid synthesis by the enzymes kynurenine aminotransferase I and II.[29] In mosquitoes, this pathway comprises the tryptophan degradation, taking to the chemically stable xanthurenic acid (XA). This acid is synthesized from the 3-HK in an irreversible reaction catalyzed by the enzyme 3-hydroxykynurenine transaminase (HKT).[30–33] The absence of kynureninase in mosquitoes makes HKT the only enzyme responsible for 3-HK regulation in mosquitoes.[33] Further, previous reports have shown that xanthurenic acid is essential for the sexual reproduction of *Plasmodium falciparium* in the malaria vector *Anopheles* spp.[34] Therefore, inhibition of the enzymatic conversion of 3-HK into xanthurenic acid in the kynurenine pathway is an attractive strategy to control *Ae. aegypti* development and *Anopheles* spp. via the accumulation of 3-HK.

Recently, the three-dimensional structure of HKT from *Ae. aegypti* in its holo form was solved. However, the crystallographic structure of HKT from *Anopheles gambiae* (AgHKT) co-crystallized with the competitive inhibitor 4-(2-aminophenyl)-4-oxobutyric acid (4-OB) was previously determined at 2.7 Å resolution.[35] These HKTs from *An. gambiae* and *Ae. aegypti* are orthologs with 79% of sequence identity, and identical residues within a radius of 7 Å from the active site.[36] Therefore, the X-ray structure of HKT from *An. gambiae* may provide valuable structural information for the design of inhibitors against HKT from *Ae. aegypti*.[36] Previously, we have recognized the striking structural similarity between 4-(2-aminophenyl)-4-oxobutyric acid inhibitor and 1,2,4-oxadiazole derivatives (Fig. 1). We have shown that these heterocyclic compounds could have similar binding modes and equivalent affinity for HKT as the crystallographic inhibitor 4-(2-aminophenyl)-4-oxobutyric acid. Furthermore, toxicity bioassays performed for fourth-instar larvae of *Ae. aegypti* have shown that several 1,2,4-oxadiazole derivatives exhibit potent activity against *Ae. aegypti* larvae (ca. of 15 ppm) and low toxicity in mammals.[36]

In this work, we report the discovery of 1,2,4-oxadiazole as inhibitors of HKT from *Ae. aegypti*. We developed a high yield procedure for the expression and purification of an active recombinant form of HKT and a biochemical protocol for the detection of the xanthurenic acid yielded by HKT catalysis. We subsequently performed enzyme inhibitory assays using the recombinant HKT and a series of novel, water-soluble, 1,2,4-oxadiazole derivatives. This work provides direct evidence that HKT can be explored as a molecular target for the discovery of novel larvicides against *Ae. aegypti*.

2. Results and discussion

2.1. In silico analysis of HKT

Gene analysis of *Aedes aegypti* HKT showed that it has four introns and five exons. For reasons of splicing processing in the prokaryotic expression system and the size of the introns in this species, it was necessary to use the cDNA for ligase independent cloning (LIC). The HKT mRNA sequence was obtained from the GenBank (access number AF435806.1) and has 1167-base pairs (bp) length. Oligonucleotides were designed from this sequence to perform a ligase independent cloning (LIC) into the expression vector. Annotation of respective translated mRNA (access number AAL29468.1) has 389 amino acids and predicted size of 43 kDa. Residues G25, S43 and R356 are located in the active site and are conserved in relation to HKT orthologs from *An. gambiae*.

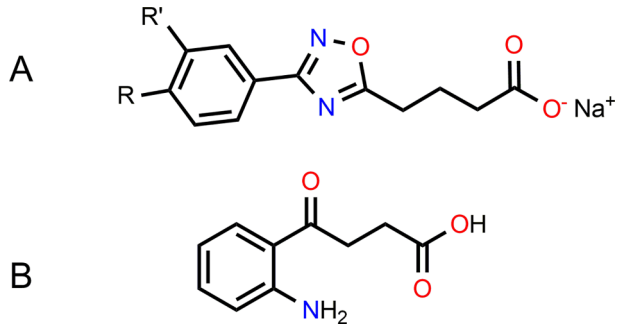

Fig. 1. Structure of (A) 1,2,4-oxadiazole scaffold and (B) 4-(2-aminophenyl)-4-oxobutyric acid (4-OB).

2.2. cDNA amplification via RT-PCR

RT-PCR was performed using total RNA extracted from pools of fourth-instar RecLab (RL) *Ae. aegypti* larvae. Samples were submitted to the reaction and a fragment of around 1100-bp was amplified. The fragments were purified, cloned in pGEM-T Easy© vector and sequenced to confirm their identity and to evaluate the integrity of these cDNA sequences. The translated protein sequences from *Ae. aegypti* HKT (RL_AeHKT) cDNA constructs were aligned with HKT sequence deposited in UniProtKB (Q95V15). The sequences showed to be identical to the reference except for a polymorphism H360M detected in all clones (Fig. 2). This mutation is provoked by the deletion of one cytosine, which caused a change in the reading frame, altering some following amino acids from these sequences. The recombinant RL AeHKT differs in ATG codon for translated methionine in comparison to the CATG codon for translated histidine from the reference sequence Q95V15 AeHKT. This polymorphism in clones that have a quite distinct geographical origin is an evidence that this mutation is well established within the species.[37] Four constructs were obtained and two of them were selected for cloning into the pETTrxA-1a/LIC expression vector.

2.3. Expression and purification of recombinant HKT

Rosetta 2 *DE3 Escherichia coli* cells transformed with the constructs were inoculated into the auto-inducer ZYM-5052 culture medium.[38] Bacterial growth was performed at 37 °C until reach OD_{600} of 0.6 and then the temperature was decreased to 22 °C to induce protein expression. The recombinant RL AeHKT is *N*-terminally fused to Thioredoxin A (Trx) and a 6x-His tag to increase the solubility of the protein, and to allow its purification by Immobilized Metal Affinity Chromatography (IMAC), respectively. The purification protocol was based on Ni^{2+} affinity chromatography to extract the recombinant HKT from bacterial lysate and subsequently, incubation with TEV protease to remove Trx and 6x-His tags. RL_AeHKT-Trx exhibited a migration profile of approximately 50 kDa, which is consistent with the predicted size of 54 kDa (43 kDa[32] of HKT e 11 kDa of Trx[39]). After all the purification steps, RL_AeHKT showed integrity at the electrophoresis level (Fig. 3) and a yield of 30 mg *per* liter of induced bacterial culture.

2.4. Synthesis of 1,2,4-oxadiazoles-like sodium salts

1,2,4-Oxadiazoles are five-membered heterocyclic compounds, which contain an oxygen atom in position 1, and two nitrogen atoms in positions 2 and 4 (Fig. 1). The oxadiazole moiety is resistant to hydrolysis and can act as a bioisostere of esters and amides, being a promising scaffold for the design of bioactive molecules. Previous studies performed by our group have shown that larvicides containing the 1,2,4-oxadiazole group could be potentially used as inhibitors of the HKT enzyme[36]. The water-soluble larvicides were obtained via a three-step synthesis, starting with the respective amidoxime and glutaric anhydride to form 4-[3-(aryl)-1,2,4-oxadiazole-5-yl]butanoic acids. After recrystallization, these compounds reacted with sodium hydroxide in methanolic medium yielding the corresponding sodium salts, which were tested for inhibitory activity against HKT (Scheme 1). Most of the compounds 3a-k was already tested as larvicides against *Aedes aegypti* by our group, but there is no report of larvicidal activity of the

A

```
1 - ATG AAA TTT ACC CCG CCG CCA AGT TCC CTC CGG GGG CCA CTC GTC ATC CCG GAC AAG ATC - 60
1 - M  K  F  T  P  P  P  S  S  L  R  G  P  L  V  I  P  D  K  I - 20

61 - ATG ATG GGC CCG GGG CCG TCC AAC TGT TCG AAA CGT GTC CTC GCG GCG TTG AAC AAC ACC - 120
21 - M  M  G  P  G  P  S  N  C  S  K  R  V  L  A  A  L  N  N  T - 40

121 - TGC CTC AGC AAC TTC CAC GAC GAG CTG TTC CAG GTC ATC GAC GAA GTC AAA GAC GGC CTG - 180
41 - C  L  S  N  F  H  D  E  L  F  Q  V  I  D  E  V  K  D  G  L - 60

181 - CGG TAC ATT TTC CAA ACC GAA AAC CGA ACC ACC ATG TGC ATC ACC GGT TCG GCT CAC ACC - 240
61 - R  Y  I  F  Q  T  E  N  R  T  T  M  C  I  T  G  S  A  H  T - 80

241 - GGC ATG GAA GCT CTG CTG TGC AAT CTA CTG GAA GAG GGA GAC ATC GTA CTC ATC GCC AAC - 300
81 - G  M  E  A  L  L  C  N  L  L  E  E  G  D  I  V  L  I  A  N - 100

301 - AAC GGT ATC TGG GCA GAG CGA GCG ATC AAT ATG GCC ACC CGA TAT GGA GCG GAC GTC CGG - 360
101 - N  G  I  W  A  E  R  A  I  N  M  A  T  R  Y  G  A  D  V  R - 120

361 - GTA TTG GAG GGA CCG GCC GAC AAA CCT TTC TCG ATG ACC GAT TTC AAA AAA GCG ATC GAA - 420
121 - V  L  E  G  P  A  D  K  P  F  S  M  T  D  F  K  K  A  I  E - 140

421 - CAA CAC AGG CCG AAA TGT CTG TTC GTA GTT CAT GGA GAC TCG TCT TCT GGA CTT CTC CAA - 480
141 - Q  H  R  P  K  C  L  F  V  V  H  G  D  S  S  S  G  L  L  Q - 160

481 - CCT CTG GAA GGT CTG GGG AAA ATC TGC CAC GAC TAT GAC TGC CTT CTG CTC GTA GAT GCC - 540
161 - P  L  E  G  L  G  K  I  C  H  D  Y  D  C  L  L  L  V  D  A - 180

541 - GTG GCT AGC CTT TGT GGT GTC CCG TTC TAC ATG GAC AAA TGG GAG ATC GAT GGC GTC TAT - 600
181 - V  A  S  L  C  G  V  P  F  Y  M  D  K  W  E  I  D  G  V  Y - 200

601 - ACC GGG TCA CAG AAG GTG CTG GGA GCC CCA CCT GGA ATA ACG CCC ATT TCC ATC AGC CCG - 660
201 - T  G  S  Q  K  V  L  G  A  P  P  G  I  T  P  I  S  I  S  P - 220

661 - AAA GCA TTA GAA GTA ATT CGG TCA CGA AAA ACG CCA TCC AAA GTA TTC TAC TGG GAC CTG - 720
221 - K  A  L  E  V  I  R  S  R  K  T  P  S  K  V  F  Y  W  D  L - 240

721 - TTA ATC TTG GGC AAC TAC TGG GGA TGC TAC GAC GAG CAG AAA CGT TAT CAT CAC ACC GTG - 780
241 - L  I  L  G  N  Y  W  G  C  Y  D  E  Q  K  R  Y  H  H  T  V - 260

781 - CCT TCC AAC CTG ATA TTT GCT CTC CGG GAA GCC ATA GCC CAG ATA GCT GAA GAA GGT CTT - 840
261 - P  S  N  L  I  F  A  L  R  E  A  I  A  Q  I  A  E  E  G  L - 280

841 - GAG CCA GTC ATA CGG CGA AGA CAG GAA TGT GCC GAG CAA ATG TAT CGC GGT CTG CAG GCA - 900
281 - E  P  V  I  R  R  R  Q  E  C  A  E  Q  M  Y  R  G  L  Q  A - 300

901 - ATG GGT TTA GAA ATA TTC GTC AAA GAT CCC GAG TAC CGG TTA CCG ACC GTG ACC TGT ATT - 960
301 - M  G  L  E  I  F  V  K  D  P  E  Y  R  L  P  T  V  T  C  I - 320

961 - ATG ATC CCA AAG GGC GTC AAC TGG TGG AAG GTC TCC GAA TAC GCC ATG AAC AAC TTT TCG - 1020
321 - M  I  P  K  G  V  N  W  W  K  V  S  E  Y  A  M  N  N  F  S - 340

1021 - CTG GAG ATC CAG GGT GGA TTT GGC CCG ACG ATG GGA ATT GCG TGG CGA GCT GGT ATC ATG - 1080
341 - L  E  I  Q  G  G  F  G  P  T  M  G  I  A  W  R  A  G  I  M - 360

1081 - GGC GAG AGT TCA ACA CTT CAG CGG GTA AAC TTC TAT CTG TAT GCG TTC AAG GAA TCT CTC - 1140
361 - G  E  S  S  T  L  Q  R  V  N  F  Y  L  Y  A  F  K  E  S  L - 380

1141 - AAA GCT ACC CAT CCG GAT TAC GTA - 1166
381 - K  A  T  H  P  D  Y  V - 400
```

Fig. 2. Open reading frame (ORF) coding sequence for the recombinant RL AeHKT and the corresponding translated amino acid sequence, showing predicted molecular weight of 43,427 Daltons. Residues from polymorphism H360M are colored with blue (A). Predicted *Aedes aegypti* HKT protein sequence from UniProtKB (Q95V15) aligned with clones RL_AeHKT1 and RL_AeHKT2. Semi- and non-conserved amino acids are colored with green and orange background, respectively. Red arrows indicate the conserved amino acids participating in substrate and inhibitor recognition in the HKT active site, as revealed by the crystal structure of AgHKT in complex with the inhibitor 4-OB[35] (B). Sequence alignment of C-terminal regions (from amino acid number 340) of RL_AeHKT1, Q95V15 and *Anopheles gambiae* HKT amino acid sequence from UniProtKB (Q7PRG3). Semi-conserved amino acids in green background and non-conserved amino acids in orange background (C).

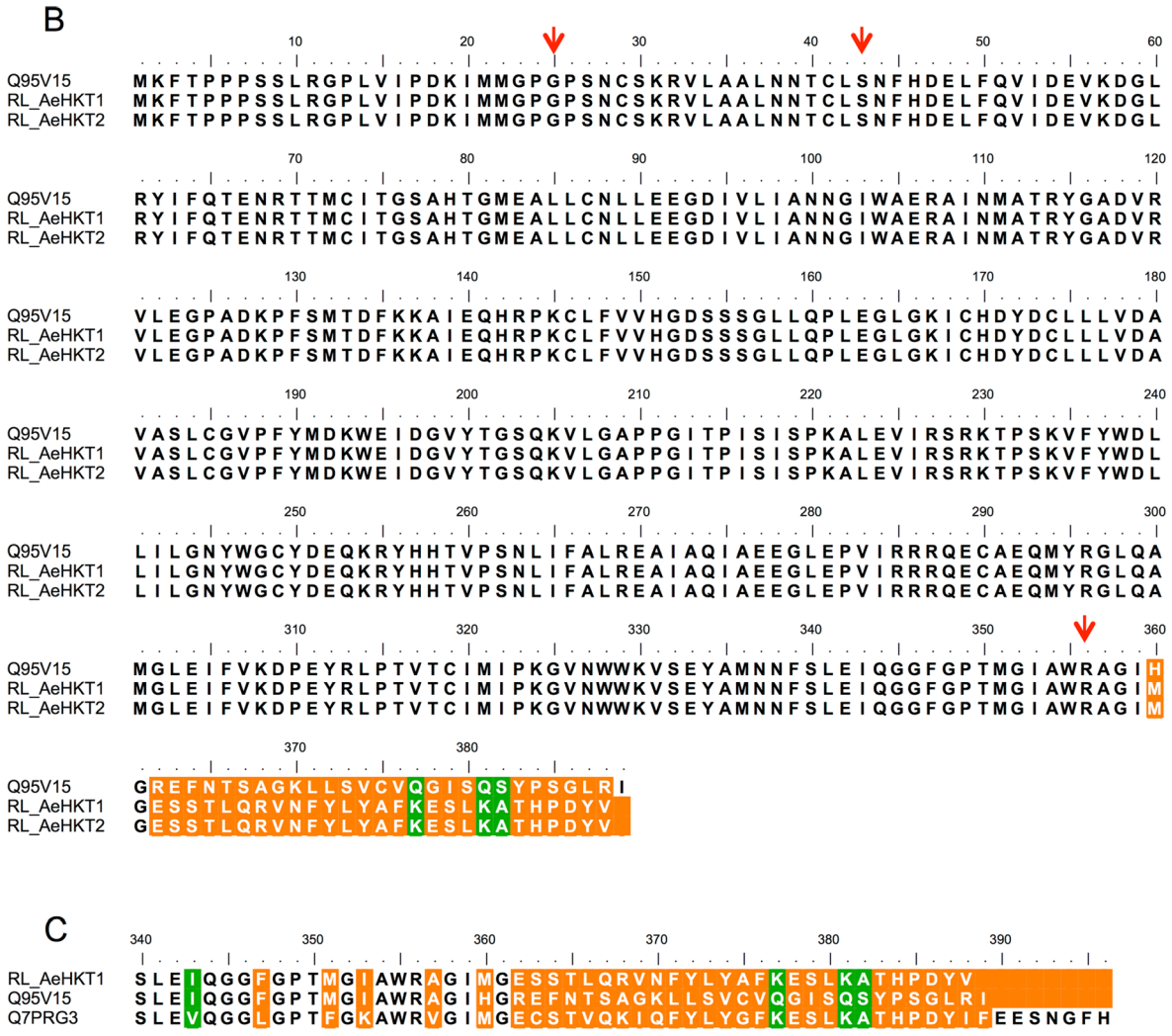

Fig. 2. (*continued*)

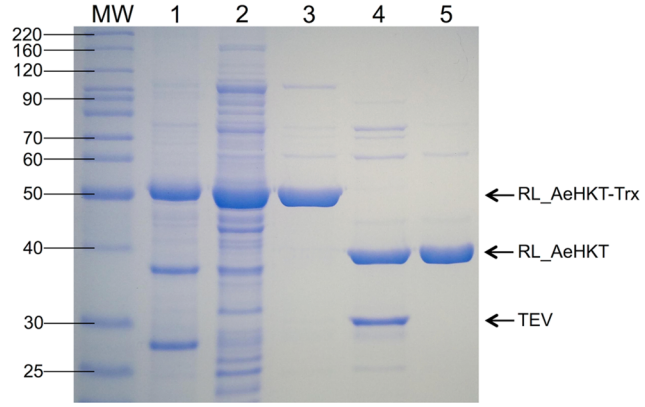

Fig. 3. SDS-PAGE-based analysis of samples collected along the purification steps of recombinant RL_AeHKT-Trx. (1) Total lysate; (2) Soluble fraction before affinity column; (3) RL_AeHKT-Trx eluted fraction by a Ni^{2+} affinity chromatography; (4) Removal of the fusion protein by TEV protease (33 kDa); (5) RL_AeHKT eluted fraction by a Ni^{2+} affinity chromatography. SDS-PAGE 10% stained with Coomassie blue. The tagged protein (RL_AeHKT-Trx), cleaved protein (RL_AeHKT) and protease used (TEV) are indicated with arrows. Molecular markers (MW) in kDa.

compounds 3c, 3e, 3g, 3h and their salt-derivatives. Since they are a series derived from canonical 3a (LC_{50} = 92.7 ppm), we can infer that the salt-derivatives 4a-k show larvicidal activity as well.[36]

2.5. Biochemical assays

Enzymatic assays were conducted by a new standardized protocol modified from Han and coworkers[32] and developed to evaluate the conversion of 3-HK to xanthurenic acid (XA) by HKT. The assays were performed on a 96-well round bottom microplate, allowing for simultaneous reading of multiple samples, and thus for a faster and cheaper characterization of RL AeHKT activity and/or inhibition. The method is based on XA-Fe^{3+} complex detection, first described by Lepkovski and coworkers to detect XA in pyridoxine-deficient mice.[40,41] More recently, Lima and coworkers used the same complexation reaction to quantify XA in *Ae. aegypti* midgut.[42] The reaction was set by the combination of 2 µg of recombinant enzyme RL_AeHKT, 2 mM of amino donor substrate (3-D,L-HK), 2 mM of amino acceptor sodium pyruvate and 40 µM of the cofactor pyridoxal-5′-phosphate (PLP) in a 100 µL final volume. Reactions were stopped by addition of 100 µL of a 10 mM $FeCl_3{\cdot}6H_2O$ solution in 0.1 M HCl. The assays were performed in duplicate, and a calibration curve was built to quantify the amount of XA generated by RL_AeHKT (R^2 = 0.98). The absorbance values of the complex were read at 570 nm after 5 min of incubation at 50 °C. Protein samples derived from two clones obtained were tested, and no differences in XA concentrations were observed, indicating that both clones are equally functional. The blank analysis was performed to verify the specificity of the complexation of Fe^{3+} to XA, instead of other components such as PLP or pyruvate. Although the mutation H360M is near to one of the important residues on the active site (R356), the

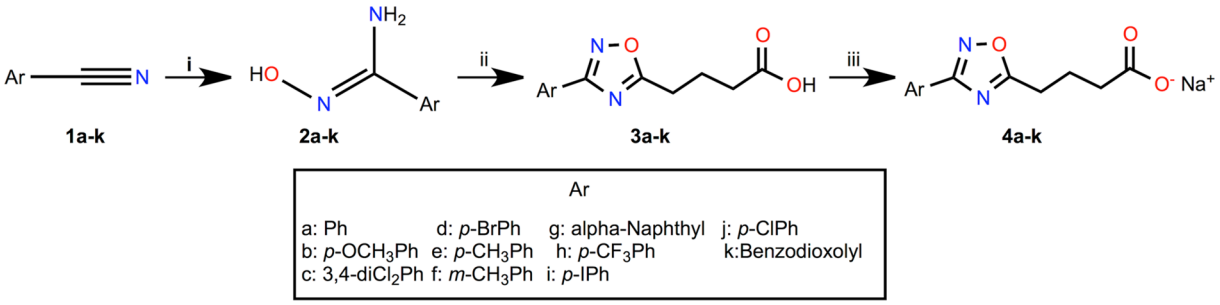

Scheme 1. Synthesis of oxadiazole salts tested as HKT inhibitors. i: $NH_2OH.HCl$ and Na_2CO_3 (4 eq.), ethanol/H_2O, r.t.; ii: glutaric anhydride (1.5 eq.), neat; iii: NaOH (1 eq.) and methanol, r.t.

enzymatic activity of the recombinant RL_AeHKT was confirmed by the formation of XA. The stability of the purified RL_AeHKT was tested in a sample stocked in 11 mg.mL^{-1}, without glycerol at −20 °C for four months. At the enzymatic activity level, the stocked protein showed similar rate as the freshly purified protein (available in SI).

2.6. Enzyme Kinetics

The steady-state kinetic constants of RL_AeHKT were estimated from absorbance changes during the catalysis of the substrate 3-D,L-HK at pH 7.5 at 50 °C using a BIOTEK© ELx808 absorbance spectrophotometer at 570 nm. Values for Michaelis-Menten constant (K_M) and maximal enzyme turnover (*k*cat) with their standard errors were calculated by fitting the experimental measurements to the Michaelis-Menten model incorporated in GraphPad Prism7.0. Catalytic efficiency (*k*cat/K_M) values with their standard errors were obtained by fitting the experimental data to the normalized Michaelis-Menten equation. Progress curves were carried from 0 to 25 min (with 5 min interval) to determine the total reaction time in order to standardize the new protocol and estimate the kinetics constants. The interval of the first-order reaction was observed from 0 to 5 min of incubation, and a plateau was reached after 20 min. Kinetics constants were calculated using the reaction conditions described in the previous section and varying 3-D,L-HK concentrations from 0.5 to 10 mM (Table 1). Previously, Han and coworkers[32] measured the kinetics constants for HKT from *Ae. aegypti* expressed in Sf9 cells (AeHKT). Although a direct comparison of our measurements to the latter work is not straightforward due to different expression conditions and biochemical assays, we measured similar K_M values for HKT expressed in *E. coli* (K_M = 3.3 mM) compared to the enzyme expressed in Sf9 cells (K_M = 3.0 mM).[32] It indicates that there are no differences in substrate specificity between the recombinant enzymes from the prokaryotic and eukaryotic organisms. In contrast, AgHKT has higher affinity for 3-D,L-HK than both recombinant HKT from *Aedes aegypti* expressed in different systems. This difference in K_M is even more remarkable in tests with L-kynurenine as substrate. One of the probable reasons for this difference in substrate recognition is the presence of D- isomer in 3-D,L-HK commercial substrate, as discussed by Canavesi and coworkers.[43] Despite this difficulty, our interest here is the HKT detoxification activity in the conversion of 3-HK to XA, besides XA is the key compound in XA-Fe^{3+} detection. In terms of turnover rate, the measured RL_AeHKT *k*cat is almost four-times lower than the AeHKT and two-times lower than AgHKT. However, the decrease in the catalytic efficiency of recombinant HKT expressed in *E. coli* compared to the one expressed in Sf9 cells was counterbalanced by a higher yield of purified protein. Hence, the former is a recombinant protein expression system cheaper and less time-consuming than that in insect cells, which is required for further inhibitory studies by novel variants of 1,2,4-oxadiazoles currently being synthesized in our group.

The effect of pH and temperature on RL_AeHKT activity was evaluated in the range between 6 and 10 and 30 to 70 °C, respectively (Fig. 4). Optimal RL_AeHKT activity was observed at pH 8, slightly lower than pH 9 measured for the HKT recombinant expressed in Sf9 cells.[32] During the measurements, there was an atypical increase in the measured RL_AeHKT activity at pH 10 (Fig. 4). Although the pH of the solution was controlled during the conversion of 3-HK into XA by HKT, the quantification of the amount of converted XA was performed through the addition of the same volume of $FeCl_3{\cdot}6H_2O$ in HCl solution. The addition of HCl rapidly decreases the final pH of the solution. It is known that iron (III) hydroxide species are formed in acid to neutral pH, and its accumulation makes the solution turbid. Consistently, we observed that upon the addition of the HCl solution to the HKT-catalyzed reaction at pH 10, the solution changed from light green/transparent to pale white/turbid appearance. The solution remained light green and transparent in all the lower pH values investigated in this work. Another possible explanation for the apparent increase in RL_AeHKT activity at pH 10 would be the formation of iron carbonate salts in alkaline pH. These salts are insoluble and begin to precipitate, making the solution turbid and preventing accurate reading via the colorimetric assay used here. However, our measurements undoubtedly indicate that RL_AeHKT exhibits optimal enzymatic activity around pH 8 (Fig. 4), and the measurement at pH 10 was reported for the sake of scientific completeness. In temperature arrays, RL_AeHKT exhibited higher activity at 50 °C with a decrease in the enzymatic activity at temperatures above that value. Additionally, the HEPES buffer was chosen for the experiments due to its reported low interference and high stability in biological assays[45] as well as our experiments showed that RL_AeHKT is more soluble at this buffer.

Table 1
Comparison of the kinetics parameters of the RL_AeHKT from *Aedes aegypti* with the recombinant HKT expressed in insect cells and the homologue HKT from *Anopheles gambiae*.

Enzyme	Substrate	K_M (mM)	*K*cat (min^{-1})	*K*cat/K_M (min^{-1}·mM^{-1})
RL_AeHKT	3-D,L-hydroxykynurenine	3.3 ± 0.8	492.3 ± 46	149.2 ± 50
AeHKT[32]	3-D,L-hydroxykynurenine	3.0 ± 0.4	1760 ± 80	587 ± 107
AgHKT[44]	3-D,L-hydroxykynurenine	2.0 ± 0.3	988.5 ± 113	494.3 ± 80
AgHKT[43]	L-kynurenine	1.4 ± 0.2	–	–

RL_AeHKT kinetics constants were derived by using final concentrations of 3-D,L-HK of 0.5 1.75, 3.0, 4.0, 8.5 and 10 mM in the presence of 5 mM sodium pyruvate. The parameters were calculated by fitting experimental data into Michaelis-Menten regression in GraphPad Prism 7.0

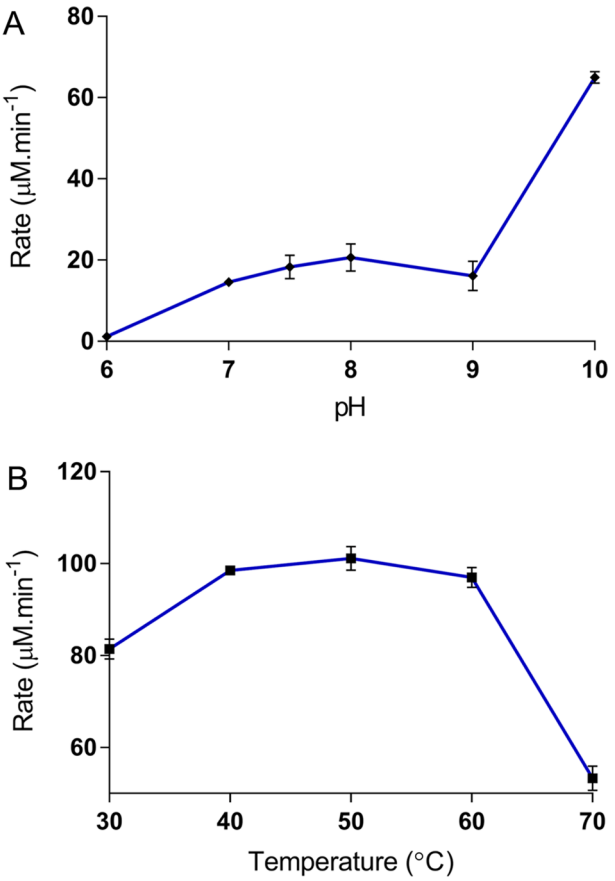

Fig. 4. Effect of pH (A) and temperature (B) on RL_AeHKT activity. The pH evaluation tests were conducted using buffers Tris-HCl pH 6, 7 and 8, HEPES pH 7.5, Borate pH 9 and Carbonate pH 10. These buffers were tested in RL_AeHKT activity during incubation time of the assay, before the addition of $FeCl_3{\cdot}6H_2O$ in HCl solution to detect XA-Fe^{3+} complex. The temperature was analyzed by incubation the complete reaction for 5 min at 30, 40, 50, 60 and 70 °C.

2.7. Inhibition assays

The inhibitory activity of eleven new 1,2,4-oxadiazole derivatives was assessed in duplicate by adding 0.5–0.05 mM of each diluted salt in 200 mM HEPES buffer pH 7/100 mM NaCl. In each assay, a negative control was taken into account to calculate the final activity percentage. The obtained IC_{50} values range from 42 to 294 μM, which are promising results for the first series of RL_AeHKT inhibitors. Eight out of the eleven inhibitors showed IC_{50} values below 100 μM (Table 2). The most potent compounds exhibited inhibition activity in the two-digits micromolar range (**4i**, IC_{50} = 42 μM and **4f**, IC_{50} = 54 μM).

Despite the chemical diversity of aromatic ring substituents in the synthesized compounds, there is not a clear relationship between the substitution pattern at the aromatic ring and the experimental IC_{50} values obtained herein (Table 2). For instance, the most promising RL_AeHKT inhibitor **4i** has an iodine atom in the *para* position, indicating that an electronegative, soft and bulky group at this position is favorable for inhibitory activity. However, inhibitors **4d** and **4j** containing bromine and chlorine atoms at the same aromatic ring position exhibited only moderate inhibition. Nevertheless, a potential structural feature associated to the increased inhibition of RL_AeHKT is the occurrence of bulky groups at the *meta* position (**4c**, **4f**, **4g**, **4k**) of compounds, exhibiting IC_{50} values bellow 100 μM (Table 2). Our previous findings indicate that chemical substitutions on the aromatic ring do not significantly affect the binding of 1,2,4-oxadiazole derivatives to HKT.[36] This is so because upon binding to the enzyme, the aromatic ring in the oxadiazole scaffold is positioned partially outside the active site pocket (Fig. 5).[36] The present findings are consistent with our previous molecular docking calculations predicting that these compounds could be potential HKT inhibitors.[36]

These assays demonstrate that 1,2,4-oxadiazole derivatives inhibit the conversion of 3-hydroxykynurenine in xanthurenic acid by the enzyme RL_AeHKT. Therefore, the next step was to determine the type of inhibition underlying this class of compounds towards RL_AeHKT. Kinetics assays were performed for four concentrations of our canonical compound **4a** at different concentrations of the substrate 3-D,L-HK (Fig. 6). Different types of inhibition can be identified from changes in the slope (V_{max}) and y-intercept location (K_M/V_{max}) of the regressions in the Lineweaver-Burk plots.[46] The addition of compound **4a** triggered changes in the regression slope and y-intercept which is representative of a noncompetitive mixed inhibition, *i.e.* it displays properties of both competitive and uncompetitive inhibitions (Fig. 6). Therefore, it can be inferred from our assay that compound **4a** decreases RL_AeHKT enzymatic activity through the binding to both the free as well as the substrate-bound enzyme. For example, this type of inhibition was observed in assays between human alanine-glyoxylate transaminase and pyruvate as inhibitor.[47] These two enzymes share 44% of identity and 67% of sequence similarity and both are PLP-dependent enzymes. The nonlinear regression fit of the raw data showed a K_i = 360 μM and αK_i = 1224 μM, indicating that the inhibitor exhibits higher affinity for the free form of the enzyme ($\alpha > 1$). The K_i value for compound **4a** is similar to the co-crystallized inhibitor from AgHKT, 4-OB (K_i = 300 μM).[35] This means that the series of compounds related here have similar behavior as the reference compound, showing potential to guide improvements aiming the development of more potent HKT inhibitors.

2.8. Potential molecular interactions of 1,2,4-Oxadiazoles with human kynurenine aminotransferase I and II

A potential undesirable protein target for 1,2,4-oxadiazoles are the human kynurenine aminotransferases I (KAT-I) and II (KAT-II). Like HKT, KATs catalyze the irreversible transamination of 3-HK to XA via a PLP-dependent transamination reaction (for a reviews see[48,49]). As per request of a Reviewer, we have applied molecular docking calculations to explore the potential binding of the canonical **4a** compound to the X-ray structures of KAT-I and KAT-II (Fig. 7). It should be mentioned that HKT and KATs have a low sequence identity (less than 20%[50,51]) and their X-ray structures exhibit RMSD values between backbone atoms of 14.6 Å for KAT-I and 10.7 Å for KAT-II (PDB ID 2VGZ[52] and 4WLH[53]). These findings suggest that HKT and KATs accumulated enough evolutive changes to have different structures, and supposedly, substrate specificity and efficiency. The molecular docking calculations for binding of the canonical compound **4a** to KAT-I and KAT-II suggest that the oxadiazole derivatives bind unspecifically to different regions of both enzymes (Fig. 7). Although compound **4a** can also bind to the active site of both enzymes, the molecule binds in a rather distinct orientation compared to the respective co-crystallized inhibitors. Furthermore, the conformers bound to the active site exhibit binding energies of the same order of magnitude as the conformers bound outside the active site. Overall, these calculations suggest that 1,2,4 oxadiazole-derivatives do not display specificity to inhibit human KAT-I and KAT-II. However, one should be cautious with the use of such simplistic computational approaches to address the rather complicated phenomena of enzyme inhibition in the absence of any experimental measurements. Experimental studies such the one presented here should be performed for human KAT-I and KAT-II in order to reliably verify if 1,2,4-oxadiazoles can inhibit these enzymes and therefore be toxic to humans.

3. Conclusions

Population control remains the only effective means to curb the

Table 2
Molecular structures of 1,2,4-oxadiazole-based inhibitors and corresponding IC_{50} and LC_{50} values.

Compound	Inhibitor	IC_{50}(μM)[a]	LC_{50}(ppm)[36,b]
4a	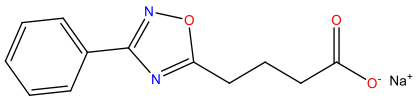	72 ± 1	92.7
4b	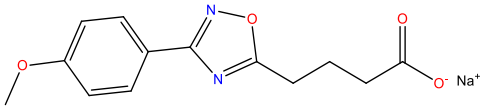	101 ± 1	> 100
4c	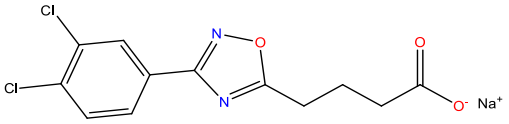	64 ± 1	–
4d	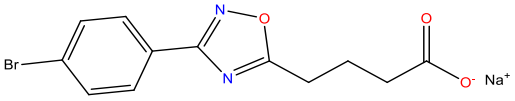	110 ± 1	10.6
4e	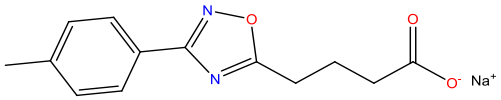	88 ± 1	–
4f	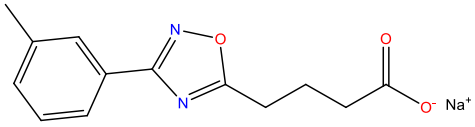	54 ± 1	75.9
4 g	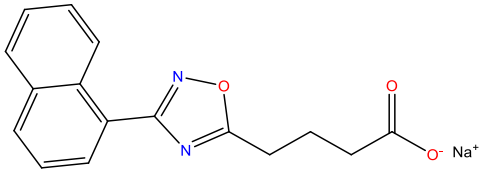	63 ± 1	–
4 h		70 ± 1	–
4i	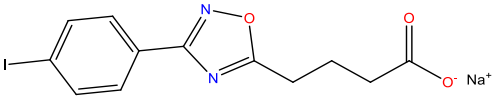	42 ± 1	16.2
4j	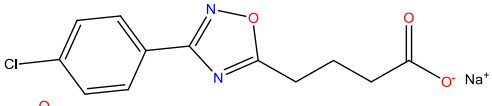	294 ± 1	34.9
4 k	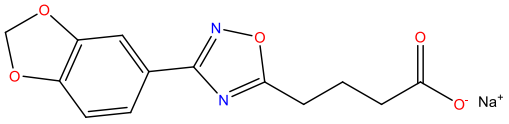	87 ± 1	72.9

[a] The compounds were tested in concentrations of 0.5, 0.25, 0.1, 0.075 and 0.05 mM. Higher concentrations of compounds 4b, 4j and 4 k were replaced by 0.45, 0.3 and 0.3 mM, respectively, to better estimate IC_{50} values. IC_{50} mean values with standard deviation.
[b] There is no report of larvicidal LC_{50} for the compounds 4c, 4e, 4 g and 4 h.

spread of most mosquito-borne diseases. This is particularly the case for *Ae. aegypti*, the transmission vector of several widespread arboviruses such as Zika, hikungunya, dengue and yellow fever. Poverty is the main determinant of arboviral infections, and even within wealthy industrialized nations, the outbreaks of arboviral transmission can arise. For instance, dengue fever, the most common arboviral infection in the world, has already spread to the continental United States.[56] Vaccines against arboviral infections are virtually nonexistent with a few exceptions (*e.g.* 17D yellow fever virus, dengue virus vaccine)[57,58]. Even though, the development of vaccines that protect against all serotypes of a given virus and/or all viruses transmitted by a given vector is a Herculean task that most likely will require time to be successfully accomplished. For this reason, current disease prevention relies on vector control interventions.

We have previously identified the enzyme 3-hydroxykynurenine transaminase (HKT) as a potential target for 1,2,4-oxadiazole derivatives with larvicidal activity against *Ae. aegypti*.[36,59,60] In insects, inhibition of HKT disrupts the detoxification metabolism of *Ae. aegypti* via the accumulation of 3-HK.[34] In the present work, we established RL_AeHKT as a molecular target for 1,2,4-oxadiazoles larvicides acting by a noncompetitive inhibition mechanism. This has been accomplished through the construction and high-yield expression of a recombinant RL_AeHKT in *E. coli*, and the standardization of a fast and low-cost absorbance spectroscopy biochemical protocol to determine HKT activity. Although the unavailability of a pure L-isomer of 3-HK in commercial sources is a limitation of this new detection method due the

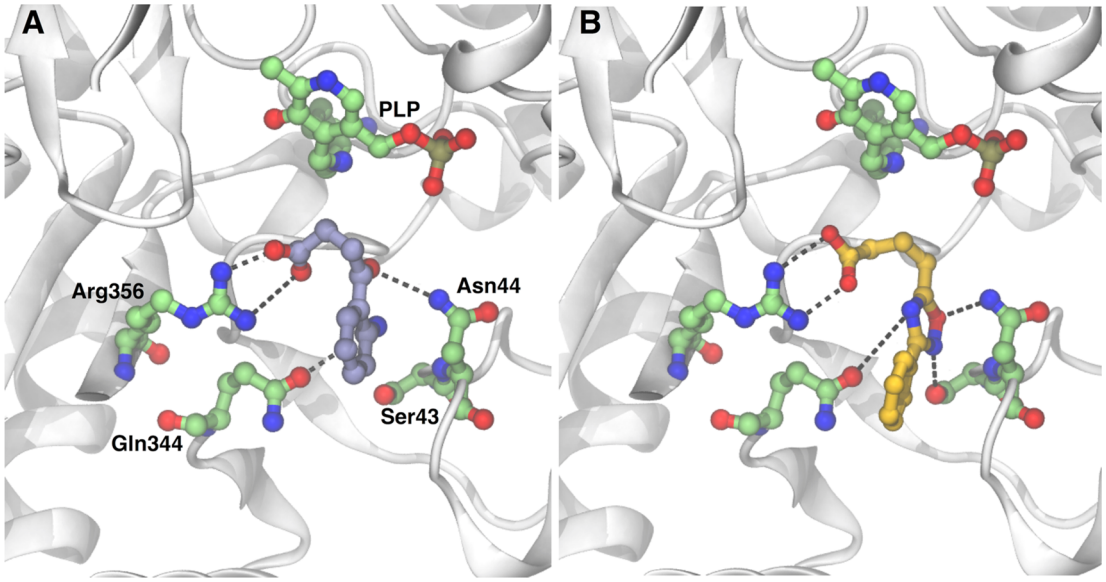

Fig. 5. Comparison of the binding mode of the co-crystallized inhibitor 4-OB (4-(2-aminophenyl)-4-oxobutyric acid) and the canonical compound **4a**. X-ray structure of *Anopheles gambiae* HKT bound to 4-OB (A) and X-ray structure with compound **4a** docked in the active site (B).[36] 4-OB is shown in lilac, compound **4a** in orange.

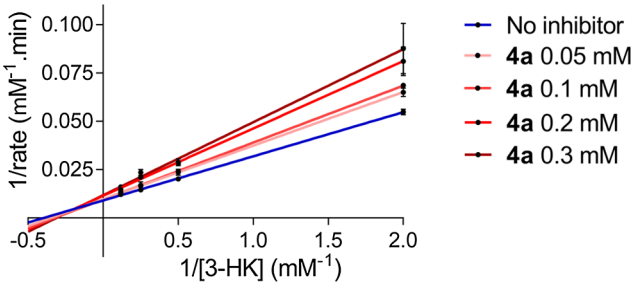

Fig. 6. Kinetics inhibitory profile of RL_AeHKT by 1,2,4-oxadiazole derivatives. The substrate 3-D,L-HK concentrations tested were 0.5, 2.0, 4.0 and 8.5 mM in 0.05, 0.1, 0.2 and 0.3 mM of inhibitor **4a**.

requirement of XA for the sensing of XA-Fe^{3+} complex, it requires a smaller amount of 3-D,L-HK (2 mM) compared to previously published assays for AeHKT and AnHKT assays (10 and 5 mM, respectively).[32,44] Moreover, the colorimetric detection dismisses the use of organic solvents as mobile phase, equipment and chromatography columns, which makes the assay so much cheaper than LC-based methods.[32,44] The analysis of HKT activity is also faster in colorimetric assays because there is no need to separate the reaction components prior to detection of XA, removing the runtime of total time of analysis. Canavesi and coworkers eliminated this drawback referent to 3-D,L-HK using L-kynurenine as substrate and LC-MS/MS detection, but this protocol still requires the chromatography separation.[43] Another issue can be testing compounds that absorbs in the range of 570 nm and this could interfere in XA-Fe^{3+} complex detection. However, only highly-conjugated organic compounds can absorbs in visible region of ultraviolet spectra, such as β-carotene (λ_{max} = 452 nm) and cyanidin chloride (λ_{max} = 545 nm) and this is not the case of 1,2,4-oxadiazoles studied here.[61]

We have produced and expressed the recombinant RL_AeHKT to evaluate the inhibitory potential and inhibitory mechanism of the previously as well as newly synthesized oxadiazole-like derivatives. The presented findings attest to the inhibitory potential of oxadiazole derivatives against the enzyme HKT, which is expected to lead to the accumulation of the highly toxic substrate 3-HK in *Ae. aegypti* larvae. Given the great structural homology between HKT from *Ae. aegypti* and *An. gambiae*, we conjecture that 1,2,4-oxadiazoles may also inhibit HKT in the latter organism.

4. Methods

In order to test the hypothesis of inhibition of synthesized oxadiazole-like compounds towards HKT, we produced the recombinant enzyme in a heterologous expression system and developed the methodology to analyze the inhibition assay. All reagents, when not specified, were purchased from Sigma-Aldrich©.

4.1. Aedes aegypti colonies

The RecLab strain of *Ae. aegypti* (from Recife – PE) kept in the insectarium from the Department of Entomology of IAM/FIOCRUZ was used. RecLab is a reference susceptible colony originated from Recife city and it was established from eggs collected in mosquito breeding sites in Recife, Brazil. This strain has been maintained for > 15 years.[62,63] To perform this experiment, 20 fourth-instar larvae were collected, washed in distilled water and kept on ice to perform RNA extraction.

4.2. RNA extraction, RT-PCR and cloning methods

Total RNA was extracted from a pool of five fourth-instar larvae using Ambion™TRIzol™ Reagent (Thermo Fischer Scientific©) and chloroform solution in water, as described by Romão, T.P. and coworkers.[64] The sample was precipitated with propan-2-ol, washed with 70% ethanol, centrifuged at 20,817 *g* for 20 min at 4 °C and suspended in DEPC water. Reverse transcription was performed at 37 °C for 1 h in a 20 μL final volume containing 5 μL of RNA treated with rDNAse, 15U reverse transcriptase AMV©, 0.5 μg Oligo dT, 1 mM each dNTP, distilled water up to 13 μL, 4 μL cDNA Synthesis Buffer and 40U RNaseOUT Recombinant Ribonuclease Inhibitor, all reagents from Invitrogen©. Two oligonucleotides were designed from the sequence deposited in GenBank accession AF435806.1 (forward primer, 5́-CAC GGATCCATGAAATTTACCCCGCCG-3́; reverse primer, 5́-CACCTCGAG AATACGTAATCCGGATGGGTAGCTTTG-3́). PCR was performed in a 25 μL final volume containing 0.25 μM each dNTP, 3U Platinum Taq DNA Polymerase from Invitrogen©, 5 μL cDNA and 0.4 μM of each primer. Each sample was amplified using a BIOMETRA© thermal cycler under the following conditions: initial denaturing at 94 °C for 3 min, then 34 cycles of denaturing at 94 °C for 50 s, annealing at 60 °C for 1 min and extension at 72 °C for 50 s followed by a final step at 72 °C for

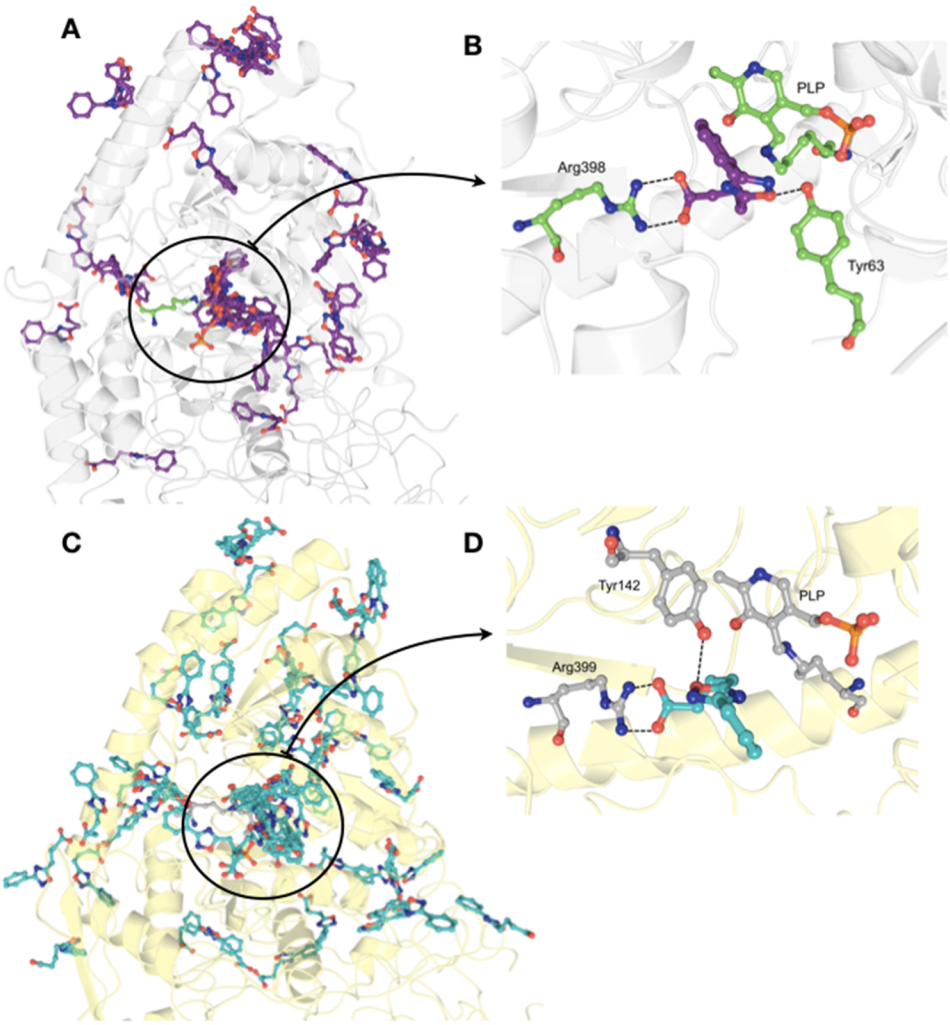

Fig. 7. Lowest energy conformations out of ca. 10^8 sampled conformations of compound **4a** upon binding to the X-ray structure of KAT-I (A) and KAT-II (C).[52–55] The molecular docking calculations cannot discriminate one single binding site of **4a** to KAT-I and KAT-II. Detail of the active site of KAT-I (B) and KAT-II (D) containing one of the multiple bound conformers of **4a**. The residues forming hydrogen-bonds or electrostatic interactions to **4a** in the respective enzymes are labeled. Compound **4a** is shown either in purple (B) or cyan(D). KAT-I is represented in white cartoon with PLP in green, and KAT-II in yellow cartoon with PLP in gray. For comparison with **4a** bound to HKT refer to Fig. 5.

10 min. PCR products were analyzed in 1% agarose electrophoresis gel. The amplified fragments were cloned into Promega© pGEM-T Easy plasmid vector and amplified. The plasmidial DNAs were purified with QIAprep Spin Miniprep kit from Qiagen© and submitted to automatic sequencing. Alignment and analysis of the nucleotide sequences were performed with BioEdit software and EditSeq from DNASTAR© package.[65,66] After confirmation, the constructs were subcloned in the plasmid pETTrxA-1a/LIC and used for the expression of the RL_AeHKT recombinant protein. Amplification of RL_AeHKT gene to add LIC overhangs were conducted in a 50 µL final volume containing 0.2 µM of each newly designed oligonucleotides (forward primer, 5́-CAGGGCGC CATGAAATTTACCCCGCCG-3́; reverse primer, 5́-GACCCGACGCGGTT ATACGTAATCCGGATGGGT-3́), 1 µL HKT-pGEM-T Easy construct, 0.2 µM each dNTP and 1U Phusion High Fidelity DNA Polymerase from Thermo Scientific©. Complementary overhangs for LIC are underlined on both primers. Each sample was amplified using a BIORAD© T100 thermal cycler under the following conditions: initial denaturing at 98 °C for 3 min, then 35 cycles of denaturing at 98 °C for 30 s, annealing at 68 °C for 30 s and extension at 72 °C for 45 s followed by a final step at 72 °C for 10 min. Insert and vector treatment and annealing were performed as described by Geerlof, A. – EBML Hamburg.[67]

4.3. Expression of recombinant HKT

The expression of the recombinant protein was carried in Rosetta 2 *DE3* cells transformed with HKT_pETTrxA-1a/LIC construct. The cultures were grown in ZYM-5052 culture medium at 37 °C until OD_{600} of 0.6 and expression was driven by incubation at 22 °C for 24 h. The cells were harvested by centrifugation of 7965*g* for 20 min at 4 °C, resuspended in lysis buffer (20 mM Tris-HCl pH 8, 200 mM NaCl, 10% glycerol, 10 mM Imidazole pH 8 and 1% Tween 20) and then lysed by sonication (8 pulses of 30 s with 45 s interval). Soluble fractions were obtained after a centrifugation of 29040*g* for 40 min at 4 °C. Protein purification steps were executed in AKTÄ pure system (GE Healthcare©). At first, ionic affinity chromatography with HisTrap HP 5 mL column was performed using buffer A (20 mM Tris-HCl pH 8, 500 mM NaCl, 20 mM Imidazole pH 8 and 10% glycerol) for column equilibration, injection and washing, followed by gradient elution with buffer B (20 mM Tris-HCl pH 8, 500 mM NaCl, 500 mM Imidazole pH 8 and 10% glycerol). The recombinant RL-AeHKT-Trx was eluted in approximately 60% of buffer B. Then, a desalting chromatography (50 mM Tris-HCl pH 8, 200 mM NaCl) with HiTrap Desalting column was made to remove imidazole excess prior to TEV cleavage. About 10% (v/v) of 2 mg/mL TEV protease was added to RL_AeHKT-Trx sample and incubated at 4 °C for 16 h. RL_AeHKT was purified from TEV and Trx mixture by another ionic affinity chromatography, and the highly purified protein was submitted to desalting and concentration by Amicon® Ultra 15 mL Centrifugal Filter – 30,000 NMWL. All the steps of expression and purification were monitored by SDS-PAGE.

4.4. Synthesis and characterization of oxadiazole salts – general methods

A series of eleven oxadiazole salts were synthesized by our research group. The reactions were monitored by TLC analysis with TLC plates

containing GF_{254} from E. Merck©. Compounds were characterized by Electro-thermal Mel-temp© apparatus to determine melting points. A Varian© UNMRS 400 MHz spectrometer, referenced as follows: ^1H (400 MHz), internal standard $SiMe_4$ at $\delta = 0.00$ ppm, ^{13}C (100 MHz), internal standard $SiMe_4$ at $\delta = 77.23$ ppm was used to obtain ^1H e ^{13}C spectra, respectively. NMR data were processed with ACD/Spectrus Processor©.[68] Elemental analyses were performed on Perkin Elmer© 2400 CHNS/O Series II Analyzer. Arylamidoximes were synthesized as described in literature.[69]

4.5. Synthesis of 4-(3-phenyl-1,2,4-oxadiazol-5-yl)butanoic acids

Glutaric anhydride (30 mmol) and the corresponding arylamidoxime (20 mmol) were put in a round-bottom flask in an oil-bath at 473 K. After one hour, the end of the reaction was verified by TLC analysis in 7:3 hexane/ethyl acetate mobile phase. Then, 10 mL of saturated $NaHCO_3$ solution and 10 mL of dichloromethane were added to the cold flask and the reaction mixture was allowed to stir overnight. After the phase separation, the aqueous phase was acidified until precipitation of the title compound occurred and then dissolved in dichloromethane, dried over Na_2SO_4 and recrystallized from a mixture of chloroform and hexane. Substances 3a,[70] 3b,[36] 3d,[71] 3e,[72] 3f,[36] 3i,[36] 3j[72] and 3k[36] were synthesized previously and their data were compared to previous literature.

4-[3-(3,4-Dichlorophenyl)-1,2,4-oxadiazol-5-yl]butanoic acid (3c) (2.8 g, 69%); mp 99–100 °C (from $CHCl_3$); ^1H NMR ($CDCl_3$, 400 MHz, $SiMe_4$) δ(ppm): 2.22 (q; 2H; J = 7.2 Hz, 7.6 Hz; CH_2); 2.57 (t; 2H; J = 7.2 Hz; CH_2); 3.05 (t; 2H; J = 7.6 Hz; CH_2); 7.55 (d; 1H; J = 8.4 Hz; Harom); 7.90 (d; 1H; J = 8.4 Hz; Harom); 8.17 (s; 1H; Harom); 10.36 (s; 1H; OH). ^{13}C NMR ($CDCl_3$, 100 MHz) δ(ppm): 21.2; 25.6; 32.8; 126.4; 126.6; 129.3; 131.0; 133.3; 135.5; 166.7; 178.5; 179.4. Elemental analysis for $C_{12}H_{10}Cl_2N_2O_3$Calcd: C, 47.86; H, 3.35; Found: C, 46.79; H, 2.85.

4-[3-(Naphthalen-2-yl)-1,2,4-oxadiazol-5-yl]butanoic acid (3 g) (2.1 g, 57%); mp 94–96 °C (from $CHCl_3$); ^1H NMR ($CDCl_3$, 400 MHz, $SiMe_4$) δ(ppm): 2.13 (q; 2H; J = 7.2 Hz, 7.6 Hz; CH_2); 2.56 (t; 2H; J = 7.2 Hz; CH_2); 2.98 (t; 2H; J = 7.6 Hz; CH_2); 7.42–7.53 (m, 3H, Harom); 7.83 (dd; 2H; J = 8.0 Hz, 8.4 Hz; Harom); 8.13 (dd; 1H, J = 0.8 Hz, 1.2 Hz; Harom); 8.78 (d; 1H; J = 8.4 Hz; Harom). ^{13}C NMR ($CDCl_3$, 100 MHz) δ(ppm): 21.3; 25.6; 32.7; 123.7; 125.0; 126.2; 126.3; 127.6; 128.6; 129.3; 130.5; 131.8; 133.8; 168.6; 177.9; 178.5. Elemental analysis for $C_{16}H_{14}N_2O_3$Calcd: C, 68.07; H, 5.00; Found: C, 67,76; H, 4,44.

4-{3-[4-(Trifluoromethyl)phenyl]-1,2,4-oxadiazol-5-yl}-butanoic acid (3 h) (1.8 g, 46%); mp 75–78 °C (from $CHCl_3$); ^1H NMR ($CDCl_3$, 400 MHz, $SiMe_4$) δ(ppm): 2.23 (q; 2H; J = 7.2 Hz, 7.6 Hz; CH_2); 2.57 (t; 2H; J = 7.2 Hz; CH_2); 3.07 (t; 2H; J = 7.6 Hz; CH_2); 7.74 (d; 2H; J = 8.0 Hz; Harom); 8.19 (d; 2H; J = 8.0 Hz; Harom); 10.40 (s; 1H; OH). ^{13}C NMR ($CDCl_3$, 100 MHz, $SiMe_4$) δ(ppm): 21.3; 25.6; 32.6; 125.6; 125.8; 127.7; 128.7; 130.1; 178.0; 178.6; 179.4. Elemental analysis for $C_{13}H_{11}F_3N_2O_3$Calcd: C, 52.01; H, 3.69; Found: C, 52.16; H, 3.38.

4.6. Synthesis of sodium 4-(3-phenyl-1,2,4-oxadiazol-5-yl)butanoate salts

In a round-bottom flask, the respective 4-(3-phenyl-1,2,4-oxadiazol-5-yl)butanoic acid (0.8 mmol) and 3.2 mL of 1% NaOH methanol solution (freshly prepared) were mixed and the reaction was allowed to stir for one hour. After the time, methanol was evaporated and the product was recrystallized from chloroform.

Sodium 4-(3-phenyl-1,2,4-oxadiazol-5-yl)butanoate (4a) (0.17 g, 89%); mp 225–226 °C (from $CHCl_3$); ^1H NMR (D_2O, 400 MHz, $SiMe_4$) δ(ppm): 1.87 (q; 2H; J = 7.2 Hz, 7.6 Hz; CH_2); 2.15 (t; 2H; J = 7.2 Hz; CH_2); 2.75 (t; 2H; J = 7.6 Hz; CH_2); 7.29–7.40 (m; 3H; Harom); 7.61 (dd; 2H; J = 7.6 Hz, 1.6 Hz; Harom). ^{13}C NMR (D_2O, 100 MHz, $SiMe_4$) δ(ppm): 25.3; 28.2; 39.2; 127.8; 129.6; 131.7; 134.3; 170.0; 183.4; 184.5. Elemental analysis for $C_{12}H_{11}N_2NaO_3$Calcd: C, 56.70; H, 4.36. Found: C, 55.93; H, 4.18.

Sodium 4-[3-(4-methoxyphenyl)-1,2,4-oxadiazol-5-yl]butanoate (4b) (0.19 g, 91%); mp 243–244 °C (from $CHCl_3$); ^1H NMR (D_2O, 400 MHz, $SiMe_4$) δ(ppm): 1.88 (q; 2H; J = 7.6 Hz, 7.6 Hz; CH_2); 2.17 (t; 2H; J = 7.6 Hz; CH_2); 2.76 (t; 2H; J = 7.6 Hz; CH_2); 3.65 (s; 3H; CH_3); 6.74 (d; 2H; J = 8.8 Hz; Harom); 7.46 (d; 2H; J = 8.8 Hz; Harom). ^{13}C NMR (D_2O, 100 MHz, $SiMe_4$) δ(ppm): 25.3; 28.2; 39.2; 57.9; 116.8; 120.4; 131.3; 163.9; 169.6; 183.1; 184.4. Elemental analysis for C13H13N2NaO4 Calcd: C, 54.93; H, 4.61. Found: C, 53.88; H, 4.66.

Sodium 4-[3-(3,4-dichlorophenyl)-1,2,4-oxadiazol-5-yl]butanoate (4c) (0.22 g, 90%); mp: 244–245 °C (from $CHCl_3$); ^1H NMR (D_2O, 400 MHz, $SiMe_4$) δ(ppm): 1.97 (q; 2H; J = 7.2 Hz, 7.6 Hz; CH_2); 2.21 (t; 2H; J = 7.2 Hz; CH_2); 2.91 (t; 2H; J = 7.6 Hz; CH_2); 7.36 (d; 1H; J = 8.8 Hz; Harom); 7.46 (dd; 1H; J = 8.8 Hz, 2.0 Hz; Harom); 7.62 (d; 1H; J = 2.0 Hz; Harom). ^{13}C NMR (D_2O, 100 MHz, $SiMe_4$) δ(ppm): 25.3; 28.3; 39.1; 127.9; 129.0; 131.1; 133.6; 135.1; 137.7; 168.4; 184.0; 184.5. Elemental analysis for $C_{12}H_9Cl_2N_2NaO_3$Calcd: C, 44.61; H, 2.81. Found: C, 43.77; H, 2.78.

Sodium 4-[3-(4-bromophenyl)-1,2,4-oxadiazol-5-yl]butanoate (4d) (0.23 g, 92%); mp 285–286 °C (from $CHCl_3$); ^1H NMR (D_2O, 400 MHz, $SiMe_4$) δ(ppm): 1.93 (q; 2H; J = 7.2 Hz, 7.6 Hz; CH_2); 2.19 (t; 2H; J = 7.2 Hz; CH_2); 2.86 (t; 2H; J = 7.6 Hz; CH_2); 7.36 (d; 2H; J = 8.4 Hz; Harom); 7.42 (d; 2H; J = 8.4 Hz; Harom). ^{13}C NMR (D_2O, 100 MHz, $SiMe_4$) δ(ppm): 25.3; 28.3; 39.2; 126.8; 128.2; 131.1; 134.6; 169.4; 183.7; 184.5. Elemental analysis for $C_{12}H_{10}BrN_2NaO_3$Calcd: C, 43.27; H, 3.03. Found: C, 42.53; H, 2,98.

Sodium 4-[3-(p-tolyl)-1,2,4-oxadiazol-5-yl]butanoate (4e) (0.18 g, 91%); mp 246–247 °C (from $CHCl_3$); ^1H NMR (D_2O, 400 MHz, $SiMe_4$) δ(ppm): 1.90 (q; 2H; J = 8.0 Hz, 7.6 Hz; CH_2); 2.16 (t; 2H; J = 7.6 Hz; CH_2); 2.22 (s; 1H; CH_3); 2.80 (t; 2H; J = 8.0 Hz; CH_2); 7.16 (d; 2H; J = 8.0 Hz; Harom); 7.56 (d; 2H; J = 8.0 Hz; Harom). ^{13}C NMR (D_2O, 100 MHz, $SiMe_4$) δ(ppm): 23.2; 25.3; 28.2; 39.1; 125.0; 129.7; 132.3; 145.3; 170.1; 183.4; 184.6 Elemental analysis for $C_{13}H_{13}N_2NaO_3$Calcd: C, 58.21; H, 4.88. Found: C, 57.53, H, 4.57.

Sodium 4-[3-(m-tolyl)-1,2,4-oxadiazol-5-yl]butanoate (4f) (0.15 g, 83%); mp 244–245 °C (from $CHCl_3$); ^1H NMR (D_2O, 400 MHz, $SiMe_4$) δ(ppm): 1.91 (q; 2H; J = 7.6 Hz, 7.2 Hz; CH_2); 2.18 (t; 2H; J = 7.2 Hz; CH_2); 2.22 (s, 1H, CH_3); 2.82 (t; 2H; J = 7.6 Hz; CH_2); 7.51–7.24 (m; 4H; Harom). ^{13}C NMR (D_2O, 100 MHz, $SiMe_4$) δ(ppm): 23.0; 25.2; 28.2; 38.9; 126.7; 127.9; 130.1; 131.6; 135.0; 141.9; 170.2; 183.4; 184.3. Elemental analysis for $C_{13}H_{13}N_2NaO_3$Calcd: C, 58.21; H, 4.88. Found: C, 56.58; H, 4.69.

Sodium 4-[3-(naphthalen-2-yl)-1,2,4-oxadiazol-5-yl]butanoate (4 g) (0.18 g, 79%); mp 195–197 °C (from $CHCl_3$); ^1H NMR (D_2O, 400 MHz, $SiMe_4$) δ(ppm): 1.80 (q; 2H; J = 7.2 Hz, 8.0 Hz; CH_2); 2.11 (t; 2H; J = 7.2 Hz; CH_2); 2.67 (t; 2H; J = 8.0 Hz; CH_2); 7.16–7.25 (m; 4H; Harom); 7.54 (dd; 2H; J = 7.2 Hz, 7.6 Hz; Harom); 8.08 (d; 1H; J = 7.6 Hz; Harom). ^{13}C NMR (D_2O, 100 MHz, $SiMe_4$) δ(ppm): 25.1; 28.1; 38.9; 124.9; 127.6; 127.6; 129.0; 130.0; 131.1; 131.5; 132.3; 134.4; 135.9; 170.0; 182.3; 184.2. Elemental analysis for $C_{16}H_{13}N_2NaO_3$Calcd: C, 63.16; H, 4.31. Found: C, 60.94; H, 4.19.

Sodium 4-[3-(4-(trifluoromethyl)phenyl)-1,2,4-oxadiazol-5-yl] butanoate (4 h) (0.22 g, 90%); mp 277–278 °C (from $CHCl_3$); ^1H NMR (D_2O, 400 MHz, $SiMe_4$) δ(ppm): 1.95 (q; 2H; J = 7.2 Hz, 7.6 Hz; CH_2); 2.19 (t; 2H; J = 7.2 Hz; CH_2); 2.88 (t; 2H; J = 7.6 Hz; CH_2); 7.60 (d; 2H; J = 8.4 Hz; Harom); 7.79 (d; 2H; J = 8.4 Hz; Harom). ^{13}C NMR (D_2O, 100 MHz, $SiMe_4$) δ(ppm): 25.3; 28.3; 39.1; 124.9; 127.6; 128.5; 128.6; 130.1; 131.5; 134.7; 135.1; 169.3; 184.0; 184.5. Elemental analysis for $C_{13}H_{10}F_3N_2NaO_3$Calcd: C, 48.46; H, 3.13. Found: C, 46.24; H, 3,09.

Sodium 4-[3-(4-iodophenyl)-1,2,4-oxadiazol-5-yl]butanoate (4i) (0.25 g, 88%); mp 285–286 °C (from $CHCl_3$); ^1H NMR (D_2O, 400 MHz, $SiMe_4$) δ(ppm): 1.96 (q; 2H; J = 7.6 Hz, 7.6 Hz; CH_2); 2.20 (t; 2H; J = 7.6 Hz; CH_2); 2.90 (t; 2H; J = 7.6 Hz; CH_2); 7.40 (d; 2H; J = 7.6 Hz; Harom); 7.68 (d; 2H; J = 7.6 Hz; Harom). ^{13}C NMR (D_2O,

100 MHz, $SiMe_4$) δ(ppm): 25.3; 28.3; 39.1; 100.6; 127.5; 131.1; 140.8; 169.7; 183.8; 184.5. Elemental analysis for $C_{12}H_{10}IN_2NaO_3$Calcd: C, 37.92; H, 2.65. Found: C, 37.88; H, 2,85.

Sodium 4-[3-(4-chlorophenyl)-1,2,4-oxadiazol-5-yl]butanoate (4j) (0.19 g, 89%); mp 277–278 °C (from $CHCl_3$); ^{1}H NMR (D_2O, 400 MHz, $SiMe_4$) δ(ppm): 1.96 (q; 2H; J = 7.6 Hz, 7.2 Hz; CH_2); 2.19 (t; 2H; J = 7.2 Hz; CH_2); 2.89 (t; 2H; J = 7.6 Hz; CH_2); 7.39 (dd; 2H; J = 7.6 Hz, 2.0 Hz; Harom); 7.67 (dd; 2H; J = 7.6 Hz, 2.0 Hz; Harom). ^{13}C NMR (D_2O, 100 MHz, $SiMe_4$) δ(ppm): 25.3; 28.3; 39.1; 126.7; 131.2; 131.8; 139.8; 169.5; 183.8; 184.6. Elemental analysis for $C_{12}H_{10}ClN_2NaO_3$Calcd: C, 49.93; H, 3.49. Found: C, 48.29; H, 3.33.

Sodium 4-[3-(benzo[d][1,3]dioxol-5-yl)-1,2,4-oxadiazol-5-yl]butanoate (4 k) (0.19 g, 87%); mp 257–259 °C (from $CHCl_3$); ^{1}H NMR (D_2O, 400 MHz, $SiMe_4$) δ(ppm): 1.92 (q; 2H; J = 7.6 Hz, 7.2 Hz; CH_2); 2.18 (t; 2H; J = 7.6 Hz; CH_2); 2.83 (t; 2H; J = 7.2 Hz; CH_2); 5.87(s; 2H; CH_2); 6.73 (d; 1H; J = 8.4 Hz; Harom); 7.03 (d; 1H; J = 1.6 Hz; Harom); 7.20 (dd; 1H; J = 8.4 Hz, 1.6 Hz; Harom). ^{13}C NMR (D_2O, 100 MHz, $SiMe_4$) δ(ppm): 25.3; 28.2; 39.1; 104.5; 109.4; 111.3; 121.7; 124.9; 150.2; 152.5; 169.7; 183.3; 184.5. Elemental analysis for $C_{13}H_{11}N_2NaO_5$Calcd: C, 56.73; H, 4.03. Found: C, 51.26; H, 3,70.

4.7. Biochemical assay

The developed method for the enzymatic assay was adapted from Han and coworkers.[32] Stock solutions were freshly prepared, except for 3-hydroxy-D,L-kynurenine (3-D,L-HK) which was kept in −20 °C. 3-D,L-HK and sodium pyruvate were directly diluted in 200 mM HEPES buffer pH 7.5/100 mM NaCl, while 20 mM pyridoxal 5′-phosphate (PLP) was first dissolved in 0.1 M NaOH and then diluted in HEPES/NaCl buffer until 0.5 mM. A solution of 20 mM xanthurenic acid was prepared in 0.1 M NaOH to perform calibration curves. The reactions were carried out in a 96-well round bottom microplate containing 8 μL of 25 mM 3-D,L-HK, 8 μL of 0.5 mM PLP and 4 μL of 50 mM sodium pyruvate, 2 μg of recombinant RL_AeHKT and HEPES/NaCl buffer to a 100 μL final volume. The plates were incubated at 50 °C for 5 min and then 100 μL of 10 mM $FeCl_3{\cdot}6H_2O$ in 0.1 M HCl was added to interrupt the reaction and generate the XA-Fe^{3+} complex. Mixes were prepared to avoid differences between replicates. Samples were performed in duplicate and absorbances were read at 570 nm. All data were analyzed using GraphPad Prism7.0 software package using the Michaelis-Menten equation. Kinetics and inhibition parameters were determined by non-linear regression.

4.8. Kinetics analysis

Kinetics assays were performed as described above. 3-D,L-HK concentrations tested are 0.5, 1.75, 3, 4, 8.5 and 10 mM in the presence of 5 mM sodium pyruvate. pH assays were performed by adding 60% of reaction volume of 200 mM Tris-HCl buffer pH 6, 7 and 8, 200 mM Borate buffer pH 9 and 200 mM Carbonate buffer pH 10, all containing 100 mM NaCl. The effect of the temperature was evaluated by incubation of all reaction components in a heater at 30, 40, 50, 60 and 70 °C. All experiments were conducted in duplicate and blank samples were analyzed simultaneously to each read.

4.9. Inhibition assays

The inhibition assays were performed with pre-incubation of each compound in five concentrations ranging from 0.5 mM to 0.05 mM with PLP and RL_AeHKT. To achieve that, solution mixes were prepared to ensure that the same amount of enzyme and co-factor was present in the different inhibitor concentrations. Blank samples and negative controls were incubated at the same time as the samples. After 30 min of incubation at 50 °C, the samples were mixed to the other reaction components and the assays were performed as described in the Biochemical assay subsection. All compounds tested were diluted in 200 mM HEPES buffer pH 7.5/100 mM NaCl and the samples were evaluated in duplicate. In each test, the negative control was added to calculate the activity percentage. Molecular docking calculations have been performed for KAT-I and KAT-II as per request of one Reviewer without any experimental evidence to validate the simulations.

4.10. Molecular docking calculations

The hybrid search method based on the Lamarckian genetic algorithm (LGA) implemented in the suite of programs AutoDock v4.0 was used in conjunction with the semi-empirical free energy force field for the molecular docking calculations.[73,74] This energy function describes the energetics of the binding process involving two molecules in an aqueous environment using pair-wise terms to evaluate the interaction between the two molecules coupled to an empirical method to estimate the contribution of the surrounding solvent [74] Hence, the free energy of binding is given by i. the difference between the energy of the ligand and the protein in a separated unbound state and ii. the energy of the ligand-protein complex. During the conformational search, the intramolecular energetics of the transition from the unbound state to the bound conformation is evaluated for each of the molecules separately, and subsequently the intermolecular energetics of bringing the two molecules together into the bound complex is evaluated. The binding energy between two molecules is given by

$$\Delta G = (V_{bound}^{ligand-ligand} - V_{unbound}^{ligand-ligand}) + (V_{bound}^{protein-protein} - V_{unbound}^{protein-protein}) (V_{bound}^{ligand-protein} - V_{unbound}^{ligand-protein} + \Delta S_{conf}) \quad (1)$$

Eq. (1) includes four terms to describe the intramolecular energies for the bound and unbound states of the guest molecule and for the bound and unbound states of the host framework, two terms to describe the change in intermolecular energy between the bound and unbound states and a one term to represent an estimate of the conformational entropy lost upon binding.[73,74] Pair-wise atomic interactions account for dispersion/repulsion, hydrogen bonding, electrostatics, and desolvation as described

$$V = W_{wdw}\sum_{ij}\left(\frac{A_{ij}}{r_{ij}^{12}} - \frac{B_{ij}}{r_{ij}^{6}}\right) + W_{hbond}\sum_{ij}E(t)\left(\frac{C_{ij}}{r_{ij}^{12}} - \frac{D_{ij}}{r_{ij}^{10}}\right) + W_{coul}\sum_{ij}\frac{q_i q_j}{\varepsilon(r_{ij})r_{ij}} + W_{sol}\sum_{ij}(S_i V_j + S_j V_i)e^{(-r_{ij}^2/2\sigma^2)} \quad (2)$$

where W corresponds to weighting constants optimized to calibrate the empirical free energy based on a set of experimentally characterized protein complexes.[74] The 6/12 potential describes dispersion/repulsion interactions with parameters A and B taken from the Amber force field.[75] The 10/12 potential is a directional H-bond term whose interaction directionality E(t) is dependent on the angle t away from ideal bonding geometry. A screened Coulomb potential is used to describe electrostatic interactions. The fourth term is a desolvation potential based on the volume (V) of the atoms surrounding a given atom, weighted by a solvation parameter (S) and an exponential term based on the distance weighting σ. Rotatable bonds included all torsional degrees of freedom.[73,74]

Molecular docking calculations were performed using the X-ray structures of the human kynurenine aminotransferase (KAT) I and II.[52–55] During the conformational search the oxadiazole ligand were fully flexible concerning its degrees of translation, orientation and conformation with respect to the protein structure, which was kept rigid. Each sampled conformation was evaluated and ranked according to the empirical energy function (equation (2)). Grid maps with 126 × 126 × 126 points of dimension and a grid spacing of 0.20 Å (active site only) and 0.502 Å (full protein) were calculated using AutoGrid4.[76] The Amber forcefield available with the distribution of

AutoDock v4.0 was used.[75] Electrostatic interactions were evaluated with a screened Coulomb potential.[77] A desolvation potential was used which is based on the volume of the atoms surrounding a given atom, weighted by a solvation parameter and an exponential term based on the distance, with a distance weighting factor of 3.5 Å.[78]

The Lamarckian Genetic Algorithm (LGA) was used to perform the conformational search following the same protocol as previously described.[79,80] Briefly, LGA parameters were defined as follows: the initial population of random individuals had a size of 150 individuals with a maximum number of 2.5×10^6 energy evaluations and a maximum number of generations equal to 27,000. An elitism rate of 1 was applied to ensure that the top individual always survives into the next generation in conjunction with mutation and crossover rates of 0.02 and 0.08, respectively. A maximum of 300 iterations per local search was used. The probability of performing a local search on an individual was 0.06 where the maximum number of consecutive successes or failures before doubling or halving the search step was 4. A total of 200 generations were sampled. The final lowest energy structures were clustered based on a RMS positional deviation of 2.0 Å.

Declaration of Competing Interest

The authors declare that they have no known competing financial interests or personal relationships that could have appeared to influence the work reported in this paper.

Acknowledgements

We thank Dr. Roberto D. Lins for using the AKTÄ to perform HKT purifications at the Dept. of Virology, IAM-FIOCRUZ. We also thank for the insectarium support from IAM-FIOCRUZ and the Program for Technological Development in Tools for Health (PDTIS-FIOCRUZ) for the use of its automatic sequencing facilities. Financial support for this research project was provided by the Brazilian funding agencies FACEPE (APQ-0732-1.06/14), BioMol/CAPES (BioComp 23038.004630/2014-35), INCT-Fx/CNPq (465259/2014-6) and FAPESP (2013/07600-3). Molecular docking calculations were performed and included in the manuscript as requested by one of the Reviewers.

Appendix A. Supplementary material

Supplementary data to this article can be found online at https://doi.org/10.1016/j.bmc.2019.115252.

References

1. Weaver SC, Reisen WK. Present and future arboviral threats. *Antiviral Res.* 2010;85(2):328–345. https://doi.org/10.1016/j.antiviral.2009.10.008.
2. Mayer SV, Tesh RB, Vasilakis N. The emergence of arthropod-borne viral diseases: A global prospective on dengue, chikungunya and zika fevers. *Acta Trop.* 2017;166:155–163. https://doi.org/10.1016/j.actatropica.2016.11.020.
3. Sukhralia S, Verma M, Gopirajan S, et al. From dengue to Zika: the wide spread of mosquito-borne arboviruses. *Eur J Clin Microbiol Infect Dis.* 2019;38(1):3–14. https://doi.org/10.1007/s10096-018-3375-7.
4. Callender DM. Management and control of yellow fever virus: Brazilian outbreak January-April, 2018. *Glob Public Health.* 2019;14(3):445–455. https://doi.org/10.1080/17441692.2018.1512144.
5. Ventura CV, Maia M, Bravo-Filho V, Góis AL, Belfort R. Zika virus in Brazil and macular atrophy in a child with microcephaly. *Lancet.* 2016;387(10015):228. https://doi.org/10.1016/S0140-6736(16)00006-4.
6. Henriques-Souza A, de Azevedo Marques ET, Antunes de Brito CA, et al. Guillain–Barré syndrome, acute disseminated encephalomyelitis and encephalitis associated with Zika virus infection in Brazil: detection of viral RNA and isolation of virus during late infection. *Am J Trop Med Hyg.* 2017;97(5):1405–1409. https://doi.org/10.4269/ajtmh.17-0106.
7. van Aalst M, Nelen CM, Goorhuis A, Stijnis C, Grobusch MP. Long-term sequelae of chikungunya virus disease: a systematic review. *Travel Med Infect Dis.* 2017;15:8–22. https://doi.org/10.1016/j.tmaid.2017.01.004.
8. Brizzi K. Neurologic manifestation of Chikungunya virus. *Curr Infect Dis Rep.* 2017;19(2):6. https://doi.org/10.1007/s11908-017-0561-1.
9. Platt DJ, Miner JJ. Consequences of congenital Zika virus infection. *Curr Opin Virol.* 2017;27:1–7. https://doi.org/10.1016/j.coviro.2017.09.005.
10. Meneses JDA, Ishigami AC, de Mello LM, et al. Lessons learned at the epicenter of Brazil's congenital Zika epidemic: evidence From 87 confirmed cases. *Clin Infect Dis.* 2017;64(10):1302–1308. https://doi.org/10.1093/cid/cix166.
11. PAHO/WHO. *Zika cases and congenital syndrome associated with Zika virus reported by countries and territories in the Americas, 2015-2018. Cumulative cases.* 2018; 2018 Published 2018 (accessed June 17, 2019).
12. World Health Organization. *Situation report: Zika virus, microcephaly, Guillain-Barré syndrome, 10 March 2017.* 2017; 2017.
13. Liu-Helmersson J, Stenlund H, Wilder-Smith A, Rocklöv J. Vectorial capacity of *Aedes aegypti* : effects of temperature and implications for global dengue epidemic potential. Moreira LA, ed. *PLoS One.* 2014;9(3):e89783. https://doi.org/10.1371/journal.pone.0089783.
14. Goyal M, Chauhan A, Goyal V, Jaiswal N, Singh S, Singh M. Recent development in the strategies projected for chikungunya vaccine in humans. *Drug Des Devel Ther.* 2018;12:4195–4206. https://doi.org/10.2147/DDDT.S181574.
15. das Neves Almeida R, Racine T, Magalhães K, Kobinger G. Zika virus vaccines: challenges and perspectives. *Vaccines.* 2018;6(3):62. https://doi.org/10.3390/vaccines6030062.
16. Viana-Medeiros PF, Bellinato DF, Martins AJ, Valle D. Insecticide resistance, associated mechanisms and fitness aspects in two Brazilian Stegomyia *aegypti* (= *Aedes aegypti*) populations. *Med Vet Entomol.* 2017;31(4):340–350. https://doi.org/10.1111/mve.12241.
17. Bellinato DF, Viana-Medeiros PF, Araújo SC, Martins AJ, Lima JBP, Valle D. Resistance status to the insecticides temephos, deltamethrin, and diflubenzuron In Brazilian *Aedes aegypti* populations. *Biomed Res Int.* 2016;2016:1–12. https://doi.org/10.1155/2016/8603263.
18. de Araújo AP, Paiva MHS, Cabral AM, et al. Screening Aedes aegypti (Diptera: Culicidae) populations from Pernambuco, Brazil for resistance to temephos, diflubenzuron, and cypermethrin and characterization of potential resistance mechanisms. *J Insect Sci.* 2019;19(3):1–15. https://doi.org/10.1093/jisesa/iez054 (16).
19. Nkya TE, Akhouayri I, Kisinza W, David J-P. Impact of environment on mosquito response to pyrethroid insecticides: facts, evidences and prospects. *Insect Biochem Mol Biol.* 2013;43(4):407–416. https://doi.org/10.1016/j.ibmb.2012.10.006.
20. Liu N. Insecticide resistance in mosquitoes: impact, mechanisms, and research directions. *Annu Rev Entomol.* 2015;60(1):537–559. https://doi.org/10.1146/annurev-ento-010814-020828.
21. Sokhna C, Ndiath MO, Rogier C. The changes in mosquito vector behaviour and the emerging resistance to insecticides will challenge the decline of malaria. *Clin Microbiol Infect.* 2013;19(10):902–907. https://doi.org/10.1111/1469-0691.12314.
22. Kasai S, Komagata O, Itokawa K, et al. Mechanisms of Pyrethroid resistance in the dengue mosquito vector, Aedes aegypti: target site insensitivity, penetration, and metabolism. Kittayapong P, ed. *PLoS Negl Trop Dis.* 2014;86(6):e2948. https://doi.org/10.1371/journal.pntd.0002948.
23. Li J, Li G. Transamination of 3-hydroxykynurenine to produce xanthurenic acid: a major branch pathway of tryptophan metabolism in the mosquito, Aedes aegypti, during larval development. *Insect Biochem Mol Biol.* 1997;27(10):859–867. https://doi.org/10.1016/S0965-1748(97)00068-4.
24. Li J, Beerntsen BT, James AA. Oxidation of 3-hydroxykynurenine to produce xanthommatin for eye pigmentation: a major branch pathway of tryptophan catabolism during pupal development in the Yellow Fever Mosquito, *Aedes aegypti*. *Insect Biochem Mol Biol.* 1999;29(4):329–338. https://doi.org/10.1016/S0965-1748(99)00007-7.
25. Chen Y, Guillemin GJ. Kynurenine pathway metabolites in humans: disease and healthy states. *Int J Tryptophan Res.* 2009;2(1):1–19. https://doi.org/10.4137/IJTR.S2097.
26. Schwarcz R, Stone TW. The kynurenine pathway and the brain: challenges, controversies and promises. *Neuropharmacology.* 2017;112(August):237–247. https://doi.org/10.1016/j.neuropharm.2016.08.003.
27. Vazquez S, Garner B, Sheil MM, Truscott RJW. Characterisation of the major autoxidation products of 3- hydroxykynurenine under physiological conditions. *Free Radic Res.* 2000;32(1):11–23. https://doi.org/10.1080/10715760000300021.
28. Giles GI, Collins CA, Stone TW, Jacob C. Electrochemical and in vitro evaluation of the redox-properties of kynurenine species. *Biochem Biophys Res Commun.* 2003;300(3):719–724. https://doi.org/10.1016/S0006-291X(02)02917-0.
29. Sathyasaikumar KV, Tararina M, Wu H-Q, et al. Xanthurenic acid formation from 3-hydroxykynurenine in the mammalian brain: neurochemical characterization and physiological effects. *Neuroscience.* 2017;367(3):85–97. https://doi.org/10.1016/j.neuroscience.2017.10.006.
30. Han Q, Fang J, Li J. 3-Hydroxykynurenine transaminase identity with alanine glyoxylate transaminase. *J Biol Chem.* 2002;277(18):15781–15787. https://doi.org/10.1074/jbc.M201202200.
31. Han Q, Kim SR, Ding H, Li J. Evolution of two alanine glyoxylate aminotransferases in mosquito. *Biochem J.* 2006;397(3):473–481. https://doi.org/10.1042/BJ20060469.
32. Han Q, Li J. Comparative characterization of *Aedes* 3-hydroxykynurenine transaminase/alanine glyoxylate transaminase and *Drosophila* serine pyruvate aminotransferase. *FEBS Lett.* 2002;527(1–3):199–204. https://doi.org/10.1016/S0014-5793(02)03229-5.
33. Han Q, Beerntsen BT, Li J. The tryptophan oxidation pathway in mosquitoes with emphasis on xanthurenic acid biosynthesis. *J Insect Physiol.* 2007;53(3):254–263. https://doi.org/10.1016/j.jinsphys.2006.09.004.
34. Garcia GE, Wirtz RA, Barr JR, Woolfitt A, Rosenberg R. Xanthurenic acid induces gametogenesis in *Plasmodium*, the Malaria Parasite. *J Biol Chem.* 1998;273(20):12003–12005. https://doi.org/10.1074/jbc.273.20.12003.

35. Rossi F, Garavaglia S, Giovenzana GB, Arca B, Li J, Rizzi M. Crystal structure of the *Anopheles gambiae* 3-hydroxykynurenine transaminase. *Proc Natl Acad Sci.* 2006;103(15):5711–5716. https://doi.org/10.1073/pnas.0510233103.
36. Oliveira VS, Pimenteira C, da Silva-Alves DCB, et al. The enzyme 3-hydroxykynurenine transaminase as potential target for 1,2,4-oxadiazoles with larvicide activity against the dengue vector *Aedes aegypti*. *Bioorg Med Chem.* 2013;21(22):6996–7003. https://doi.org/10.1016/j.bmc.2013.09.020.
37. Matthews BJ, Dudchenko O, Kingan S, et al. Improved Aedes aegypti mosquito reference genome assembly enables biological discovery and vector control. *bioRxiv.* 2017;240747. https://doi.org/10.1101/240747.
38. Studier FW. Protein production by auto-induction in high-density shaking cultures. *Protein Expr Purif.* 2005;41(1):207–234. https://doi.org/10.1016/j.pep.2005.01.016.
39. Novagen I. pET system manual. http://research.fhcrc.org/content/dam/stripe/hahn/methods/biochem/pet.pdf. Published 1991. Accessed June 18, 2019.
40. Lepkovsky S, Roboz E, Haagen-Smit AJ. Xanthurenic acid and its role in the tryptophane metabolism of pyridoxine-deficient rats. *J Biol Chem.* 1943;149:195–201.
41. Lepkovsky S, Nielsen E. A green pigment-producing compound in urine of pyridoxine-deficient rats. *J Biol Chem.* 1942;144:135–138.
42. Lima VLA, Dias F, Nunes RD, et al. The antioxidant role of xanthurenic acid in the *Aedes aegypti* Midgut during digestion of a blood meal. Hansen IA, ed. *PLoS One.* 2012;7(6):e38349. https://doi.org/10.1371/journal.pone.0038349.
43. Canavesi R, Miggiano R, Stella M, et al. Study of Anopheles gambiae 3-hydroxykynurenine transaminase activity and inhibition by LC-MS/MS method. *J Pharm Biomed Anal.* 2019;173:154–161. https://doi.org/10.1016/j.jpba.2019.05.025.
44. Rossi F, Lombardo F, Paglino A, et al. Identification and biochemical characterization of the Anopheles gambiae 3-hydroxykynurenine transaminase. *FEBS J.* 2005;272(21):5653–5662. https://doi.org/10.1111/j.1742-4658.2005.04961.x.
45. Good NE, Winget GD, Winter W, Connolly TN, Izawa S, Singh RMM. Hydrogen ion buffers for biological research. *Biochemistry.* 1966;5(2):467–477. https://doi.org/10.1021/bi00866a011.
46. Lineweaver H, Burk D. The determination of enzyme dissociation constants. *J Am Chem Soc.* 1934;56(3):658–666. https://doi.org/10.1021/ja01318a036.
47. Cellini B, Bertoldi M, Montioli R, Paiardini A, Borri Voltattorni C. Human wild-type alanine:glyoxylate aminotransferase and its naturally occurring G82E variant: functional properties and physiological implications. *Biochem J.* 2007;408(1):39–50. https://doi.org/10.1042/BJ20070637.
48. Rossi F, Schwarcz R, Rizzi M. Curiosity to kill the KAT (kynurenine aminotransferase): structural insights into brain kynurenic acid synthesis. *Curr Opin Struct Biol.* 2008;18(6):748–755. https://doi.org/10.1016/j.sbi.2008.09.009.
49. Rossi F, Miggiano R, Ferraris DM, Rizzi M. The synthesis of kynurenic acid in mammals: an updated kynurenine aminotransferase structural KATalogue. *Front Mol Biosci.* 2019;6(February):1–9. https://doi.org/10.3389/fmolb.2019.00007.
50. Sievers F, Wilm A, Dineen D, et al. Fast, scalable generation of high-quality protein multiple sequence alignments using Clustal Omega. *Mol Syst Biol.* 2011;7(539) https://doi.org/10.1038/msb.2011.75.
51. Sievers F, Higgins DG. Clustal Omega for making accurate alignments of many protein sequences. *Protein Sci.* 2018;27(1):135–145. https://doi.org/10.1002/pro.3290.
52. Rossi F, Garavaglia S, Montalbano V, Walsh MA, Rizzi M. Crystal structure of human kynurenine aminotransferase II, a drug target for the treatment of schizophrenia. *J Biol Chem.* 2008;283(6):3559–3566. https://doi.org/10.1074/jbc.M707925200.
53. Nadvi NA, Salam NK, Park J, et al. High resolution crystal structures of human kynurenine aminotransferase-I bound to PLP cofactor, and in complex with aminooxyacetate. *Protein Sci.* 2017;26(4):727–736. https://doi.org/10.1002/pro.3119.
54. Han Q, Robinson H, Cai T, Tagle DA, Li J. Structural insight into the inhibition of human kynurenine aminotransferase I/Glutamine transaminase K. *J Med Chem.* 2009;52(9):2786–2793. https://doi.org/10.1021/jm9000874.
55. Han Q, Cai T, Tagle DA, Robinson H, Li J. Substrate specificity and structure of human aminoadipate aminotransferase/kynurenine aminotransferase ii. *Biosci Rep.* 2008;28(4):205–215. https://doi.org/10.1042/BSR20080085.
56. George SL. Prospects for a dengue vaccine: progress and pitfalls. *Mo Med.* 2014;111(3):337–342http://ovidsp.ovid.com/ovidweb.cgi?T=JS&PAGE=reference&D=emed12&NEWS=N&AN=25211865.
57. Wieten RW, Goorhuis A, Jonker EFF, et al. 17D yellow fever vaccine elicits comparable long-term immune responses in healthy individuals and immune-compromised patients. *J Infect.* 2016;72(6):713–722. https://doi.org/10.1016/j.jinf.2016.02.017.
58. Scott LJ. Tetravalent dengue vaccine: a review in the prevention of dengue disease. *Drugs.* 2016;76(13):1301–1312. https://doi.org/10.1007/s40265-016-0626-8.
59. Neves Filho RAW, da Silva CA, da Silva CSB, et al. Improved microwave-mediated synthesis of 3-(3-Aryl-1,2,4-oxadiazol-5-yl)propionic acids and their larvicidal and fungal growth inhibitory properties. *Chem Pharm Bull (Tokyo).* 2009;57(8):819–825. https://doi.org/10.1248/cpb.57.819.
60. da Silva-Alves DCB, dos Anjos JV, Cavalcante NNM, Santos GKN, Navarro DMDAF, Srivastava RM. Larvicidal isoxazoles: synthesis and their effective susceptibility towards *Aedes aegypti* larvae. *Bioorg Med Chem.* 2013;21(4):940–947. https://doi.org/10.1016/j.bmc.2012.12.006.
61. Pavia DL, Lampman GM, Kriz GS. Ultraviolet spectroscopy. *Introduction to spectrocopy – a guide for students of organic chemistry.* 2nd ed. Saunders College Publishing; 1996:267–302.
62. Kuno G. Early history of laboratory breeding of *Aedes aegypti* (Diptera: Culicidae) focusing on the origins and use of selected strains. *J Med Entomol.* 2010;47(6):957–971. https://doi.org/10.1603/ME10152.
63. Melo-Santos MAV, Varjal-Melo JJM, Araújo AP, et al. Resistance to the organophosphate temephos: mechanisms, evolution and reversion in an *Aedes aegypti* laboratory strain from Brazil. *Acta Trop.* 2010;113(2):180–189. https://doi.org/10.1016/j.actatropica.2009.10.015.
64. Romao TP, de Melo Chalegre KD, Key S, et al. A second independent resistance mechanism to *Bacillus sphaericus* binary toxin targets its alpha-glucosidase receptor in Culex quinquefasciatus. *FEBS J.* 2006;273(7):1556–1568. https://doi.org/10.1111/j.1742-4658.2006.05177.x.
65. DNASTAR. EditSeq©. 2006.
66. Hall TA. BioEdit: a user-friendly biological sequence alignment editor and analysis program for Windows 95/98/NT. *Nucleic Acids Symp Ser.* 1999;41:95–98http://jwbrown.mbio.ncsu.edu/JWB/papers/1999Hall1.pdf.
67. Geerlof A. Ligase Independent Cloning (LIC). https://doi.org/10.1002/9783527678679.dg06795.
68. Inc. ACD. ACD/Spectrus Processor. 2017. www.acdlabs.com.
69. Eloy F, Lenaers R. The chemistry of amidoximes and related compounds. *Chem Rev.* 1962;62(2):155–183. https://doi.org/10.1021/cr60216a003.
70. Huhtiniemi T, Suuronen T, Rinne VM, et al. Oxadiazole-carbonylaminothioureas as SIRT1 and SIRT2 Inhibitors. *J Med Chem.* 2008;51(15):4377–4380. https://doi.org/10.1021/jm800639h.
71. Tale RHH, Rodge AHH, Keche APP, et al. Synthesis and anti-bacterial, anti-fungal activity of novel 1,2,4-oxadiazole. *J Chem Pharm Res.* 2011;3(2):496–505.
72. Lueg C, Schepmann D, Günther R, Brust P, Wünsch B. Development of fluorinated CB2 receptor agonists for PET studies. *Bioorg Med Chem.* 2013;21(23):7481–7498. https://doi.org/10.1016/j.bmc.2013.09.040.
73. Morris GM, Huey R, Lindstrom W, et al. AutoDock4 and AutoDockTools4: automated docking with selective receptor flexibility. *J Comput Chem.* 2009;30(16):2785–2791. https://doi.org/10.1002/jcc.21256.
74. Huey R, Morris GM, Olson AJ, Goodsell DS. A semiempirical free energy force field with charge-based desolvation. *J Comput Chem.* 2007;28(6):1145–1152. https://doi.org/10.1002/jcc.20634.
75. Weiner SJ, Kollman PA, Singh UC, et al. A new force field for molecular mechanical simulation of nucleic acids and proteins. *J Am Chem Soc.* 1984;106(3):765–784. https://doi.org/10.1021/ja00315a051.
76. Goodford PJ. A computational procedure for determining energetically favorable binding sites on biologically important macromolecules. *J Med Chem.* 1985;28(7):849–857. https://doi.org/10.1021/jm00145a002.
77. Mehler EL, Solmajer T. Electrostatic effects in proteins: comparison of dielectric and charge models. *Protein Eng Des Sel.* 1991;4(8):903–910. https://doi.org/10.1093/protein/4.8.903.
78. Stouten PFW, FrÖmmel C, Nakamura H, Sander C. An effective solvation term based on atomic occupancies for use in protein simulations. *Mol Simul.* 1993;10(2–6):97–120. https://doi.org/10.1080/08927029308022161.
79. Soares TA, Goodsell DS, Briggs JM, Ferreira R, Olson AJ. Docking of 4-oxalocrotonate tautomerase substrates: implications for the catalytic mechanism. *Biopolymers.* 1999;50(3):319–328. https://doi.org/10.1002/(SICI)1097-0282(199909)50:3<319::AID-BIP7>3.0.CO;2-8.
80. Soares TA, Goodsell DS, Ferreira R, Olson AJ, Briggs JM. Ionization state and molecular docking studies for the macrophage migration inhibitory factor: The role of lysine 32 in the catalytic mechanism. *J Mol Recognit.* 2000;13(3):146–156. https://doi.org/10.1002/1099-1352(200005/06)13:3<146::AID-JMR497>3.0.CO;2-4.